Kinetic condensation of metals in the early solar system: Unveiling the cooling history of solar nebula by refractory metal nuggets

Mingen Pan (潘明恩)[*]

Department of the Geophysical Sciences, The University of Chicago, 5734 South Ellis Avenue, Chicago, IL 60637, USA
Department of Computer Science, Columbia University, 500 West 120th Street, New York, NY 10027, USA

ARTICLE INFO

ABSTRACT

Refractory Metal Nuggets (RMNs; submicrometer highly siderophile element rich metal alloys) are observed in Ca, Al-rich inclusions (CAIs) and other components of primitive meteorites, and some RMNs could have condensed from the Solar Nebula. In order to study the condensation of RMNs in the Solar Nebula, NUCON – a kinetic condensation model – has been developed to simulate the nucleation and condensation of refractory siderophile metal phases. NUCON treats RMNs as solid solutions where multiple elements can accrete onto one RMN. To achieve this goal, the homogeneous nucleation theory is modified to compute the nucleation of solid solutions. Also, a numerical method is developed to compute the integration of condensation and evaporation rates of an RMN. Equilibrium among gaseous phases is also considered, including monatomic gases and oxides. The oxygen fugacity of the simulated Solar Nebula can also be modified by adjusting carbon abundance. NUCON shows that the nucleation of RMNs was inhibited even when the cooling rate of the Solar Nebula was below 0.1 K/year, and RMNs experienced kinetic condensation largely deviated from the equilibrium condensation.

This study modeled the condensation of RMNs in the RMN-forming regions with different cooling rates, total pressures, and oxygen fugacities, and explored how these parameters affect the radii and Ni/Fe ratios of RMNs. To reproduce the RMNs reported in literature, most of which have radii from 100 to 1000 nm, the cooling rate during the accretion of refractory siderophile metals in RMN-forming regions should be in the order of 1 K/year. The timescale of refractory-metal condensation is in the order of 10^2 years. In addition, RMNs have been measured to have Ni/Fe ratios from almost zero to over unity, and NUCON shows that the cooling rate during Fe—Ni accretion in RMN-forming regions should be in the order of 10 K/h so that the observed Ni/Fe ratios of RMNs can be reproduced. The timescale of Fe—Ni condensation is in the order of 10 h. Thus, NUCON predicts a transition from slow cooling to rapid cooling that is likely to have occurred during RMN condensation.

1. Introduction

Ca, Al-rich inclusions (CAIs) in primitive meteorites have been identified as the oldest objects forming in the Solar System (Connelly et al., 2012). CAIs formed in a hot environment and experienced high-temperature processes (Ireland and Fegley Jr, 2000). One of the most likely CAI-forming regions was the inner mid-plane (<0.5 AU) of the protoplanetary disk of the Solar System, where temperatures could exceed 1500 K based on the observation of T-Tauri stars (Woolum and Cassen, 1999). Therefore, CAIs and their components may record the evolution of the inner Solar System. CAIs have distinctive mineralogy and are found in all types of chondrites except CI chondrites, and the common minerals of CAIs include hibonite, perovskite, spinel, melilite,

pyroxene, and anorthite (MacPherson, 2014). Highly siderophile elements (HSEs) were observed to be enriched in CAIs compared to solar average values (Grossman, 1973; Wänke et al., 1974). Under the redox condition of the Solar Nebula (Grossman et al., 2008), the concentration of HSEs in silicate minerals is much lower than their concentration in CAIs (Holzheid et al., 1994; Borisov and Palme, 1995, 1997; Borisov and Walker, 2000), so HSEs should be concentrated in metal-rich phases. Wark and Lovering (1976) discovered refractory metal nuggets (RMNs) with diameters of 0.5–3 μm in CAIs. At the same time, Palme and Wlotzka (1976) discovered a 20-μm, opaque assemblage enriched in refractory siderophile elements. There is ongoing discussion as to the origin of opaque assemblages (El Goresy et al., 1977; Blum et al., 1988). Opaque assemblages are multi-phase objects consisting of Fe—Ni

---

metals, HSE-rich blebs, oxides, and sometimes S, P-bearing minerals (El Goresy et al., 1978), while RMNs are homogeneous metal alloys enriched in refractory HSE (Harries et al., 2012). Besides in CAIs, RMNs have been found in all components of carbonaceous chondrites (e.g. Wang et al., 2007; Schwander et al., 2015a; Daly et al., 2017a) and also in cosmic spherules (Rudraswami et al., 2014).

Three theories have been proposed to explain the origin of RMNs: (1) condensation from the Solar Nebula or stellar environments (Wark and Lovering, 1976; Palme and Wlotzka, 1976; Berg et al., 2009; Croat et al., 2013; Daly et al., 2017a), (2) precipitation from CAI melt (Schwander et al., 2015a), or (3) secondary processing from parent bodies or nebulae (Blum et al., 1988; Palme et al., 1998; Daly et al., 2017b). The condensation theory has a long history because the mineralogy of their host CAI can be explained by equilibrium condensation (e.g., Grossman, 1972; Ebel, 2006). Palme and Wlotzka (1976) were the first ones to apply equilibrium condensation to the formation of RMN and showed that RMNs condensed at higher temperatures than the common minerals in CAIs. Sylvester et al. (1990) modeled the condensation of refractory siderophile metals into three crystal structures, but later studies found that most RMNs exist in single-crystal structure (Harries et al., 2012; Daly et al., 2017b). Berg et al. (2009) found that the refractory siderophile metals (Os, W, Mo, Ru) of RMNs seem to follow an equilibrium condensation pattern. Daly et al. (2017c) discovered some sulfidized RMNs and explained their origin by condensation from the Solar Nebula and reaction with cool S-bearing gas before being captured by a CAI. Daly et al. (2017a) observed the heterogeneous composition of RMNs and proposed that some RMNs might have been inherited by the Solar System from the Giant Molecular Cloud. Since high temperatures were unlikely to have been achieved in molecular clouds, the RMNs would have had to condense in circumstellar environments. The RMNs found in presolar grains also support the condensation origin from a circumstellar environment for a sub-population of RMNs (Croat et al., 2013). The second theory – precipitation origin – was proposed by Schwander et al. (2015a). They examined RMNs in compact/molten CAIs and demonstrated that the composition of these RMNs cannot be explained by the equilibrium condensation calculations. Synthesis experiments can also reproduce RMNs from CAI-like melts (Schwander et al., 2015b). However, this hypothesis only applies to molten CAIs. Some CAIs, like fluffy Type A inclusions (MacPherson and Grossman, 1984) and fine-grained inclusions (Krot et al., 2004), have not experienced melting, so the RMNs there, if any, cannot have formed by precipitation. Also, the precipitation theory fails to explain the Ru isotopic anomaly between RMNs and host CAIs (Fischer-Gödde et al., 2018). RMNs should have identical isotopic anomalies as host CAIs if they precipitated from the CAI melt. The third theory argues that RMNs could have been altered or even generated by the secondary processes in nebulae or on parent bodies. Blum et al. (1988) found that the opaque assemblages consisting of RMNs, oxides, and sulfides should have been formed by exsolution, oxidation, and sulfidization from metal alloys. Heating experiments confirmed that the RMNs could significantly lose Mo and W at high temperature and oxidizing environment (Palme et al., 1998). Daly et al. (2017b) analyzed the texture of a secondary Mo, W-rich phase, and found the evidence of solid state recrystallization likely due to a transient heating event in the protoplanetary disk. The RMNs associated with secondary processes consist of oxide and/or sulfide phases, making them different from the primitive RMNs forming through condensation or precipitation.

If RMNs exist in CAIs with condensate textures or CAIs that preserve condensation features, condensation models can thus be used to study their formation. Equilibrium models have been used broadly to study RMN formation (e.g., Palme and Wlotzka, 1976; Sylvester et al., 1990; Berg et al., 2009; Daly et al., 2017a). However, an equilibrium model can only describe the final state of a system and not provide direct information or the path followed to the final state. Tanaka et al. (2002) abandoned the equilibrium calculation and used the homogeneous nucleation theory to simulate the nucleation process, but they only considered the condensation of individual refractory elements separately. Since refractory siderophile metals condensed as solid solutions, the model of Tanaka et al. (2002) failed to reproduce the condensation of refractory siderophile metals into one phase. For example, the moderately refractory siderophile metal (e.g., Mo, Ru, and Ir) would prefer to condense on the preexisting grains rather than to generate new nuclei. Petaev et al. (2003) implemented the gas collision theory into equilibrium model and used the model to depict the condensation and growth of metal grains in the CH/CB chondrites, but they did not consider the nucleation inhibition generated by the surface energy. Fedkin et al. (2015) used the Hertz-Knudsen equations to model the metal condensation, but they did not quantitatively model the nucleation process and arbitrarily assumed the nuclei to be generated at the temperature 100 K below the saturation temperature.

To overcome the limitations of the previous studies, NUCON (NUcleation-CONdensation) model has been developed to simulate the gas-solid condensation process of RMNs. The mechanism of NUCON is elaborated in Section 2. Section 3 shows the results of RMN condensation in different nebula environments. Section 4 discusses the following questions: (1) How does NUCON infer the environments of RMN-forming regions from the properties of RMNs? (2) How did the environments of RMN-forming regions evolve during the condensation of RMNs? (3) How did HSEs behave during the kinetic condensation of RMNs?

2. Kinetic condensation model

NUCON consists of the following modules: gaseous equilibrium, nucleation, grain growth, and mass balance (Fig. 1). The nucleation calculation is adopted from Tanaka et al. (2002) and improved to consider the nucleation of multi-element nuclei. The grain growth (i.e. condensation and evaporation) are computed based on Hertz-Knudsen equations (e.g., Davis and Richter, 2014). RMNs are treated as solid solutions to compute condensation and evaporation rates. Since oxygen fugacity significantly affects the fugacity of W and Mo, the thermodynamic equilibrium among gaseous molecules are considered as well. In principle, solid-state diffusion should be considered, but homogenization is quickly reached at high temperature by diffusion given the size of RMNs (Supplementary Information S1), so the composition of RMNs is assumed homogeneous. Free parameters of NUCON consist of pressure, cooling rate and oxygen fugacity. The bulk composition of the initial condensing gas is assumed to be solar abundance and the oxygen fugacity is controlled by modifying the carbon abundance.

A simulated condensation process is divided into multiple steps with constant time period Δt. In the beginning of each step, the environmental parameters (temperature and pressure) and the attributes of matters (standard Gibbs free energy of formation, surface energy, number density) are updated. Second, the gaseous equilibrium module calculates the chemical equilibrium among gaseous phases. Then, the nucleation rate of RMNs is computed by the nucleation module. The newly-generated nuclei will be added into a container of condensates at the end of this step. The container of condensates records the latest attributes (e.g. composition, size, number density) of all the nuclei. In this article, a nucleus is referred to the solid that has just overcome the surface-energy barrier, and a condensate is referred to the growing/grown solid where gaseous particles have been accreting. The concept of condensate thus includes the nucleus. Next, if any condensates were generated before this step, the grain growth module will compute their growth based on Hertz-Knudsen equations. The attributes of the condensates are updated accordingly. Finally, the mass balance module adjusts the amount of gases and solids based on mass conservation.

2.1. Gaseous equilibrium

Refractory siderophile metals are resistant to oxidation except Mo and W (Fegley Jr and Palme, 1985). Besides monatomic phases, gaseous
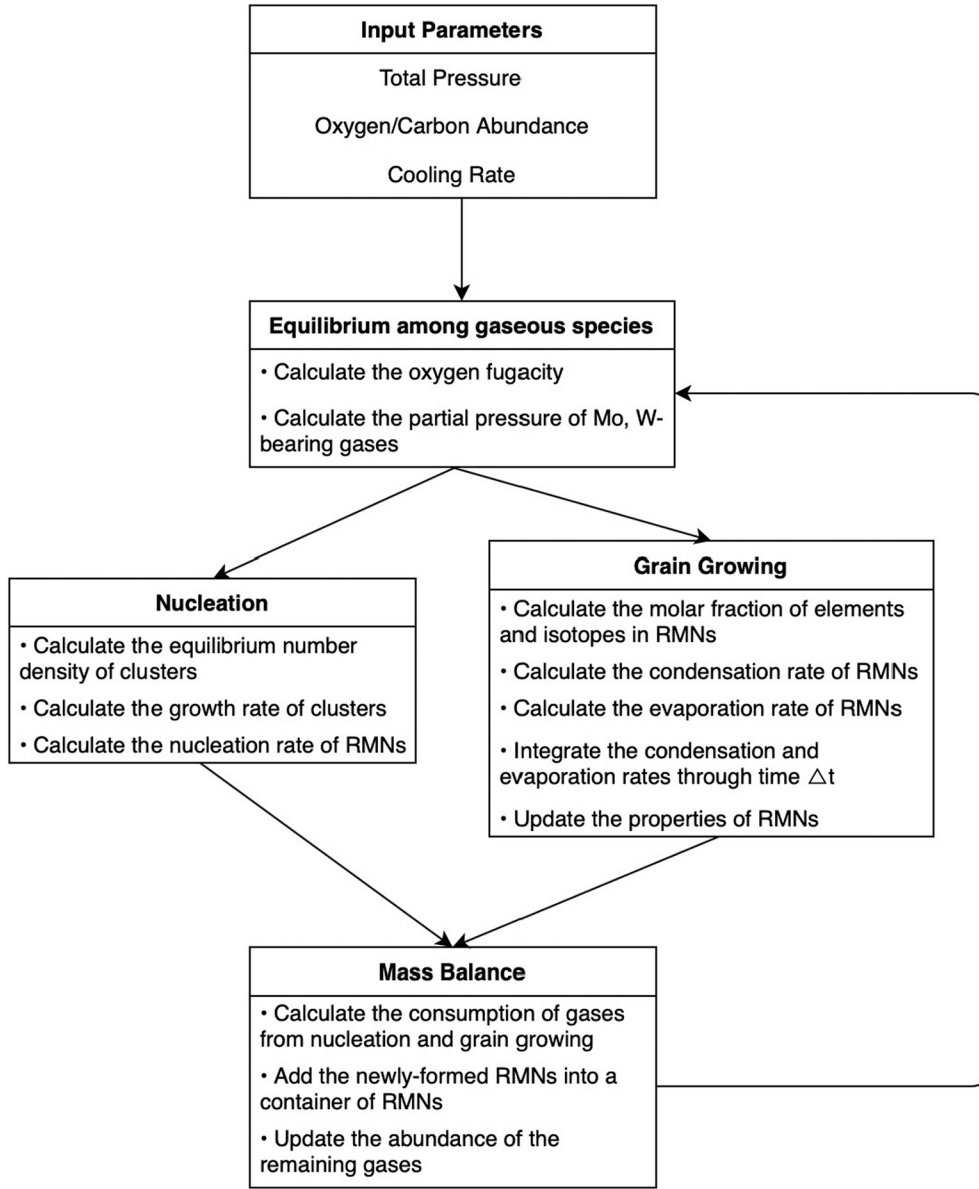
Fig. 1. The flow diagram of the kinetic condensation model – NUCON.

Mo mainly exists as MoO, MoO_2, and MoO_3; W mainly exists as WO, WO_2, WO_3, W_3O_8. They may also exist in other gaseous phases, but their abundance is too low to consider. The thermodynamic data of these phases are discussed in Supplemental Information S3. The fugacity (partial pressure) of the monatomic gases of Mo and W is mainly controlled by oxygen fugacity and temperature (Fig. 2). Given the abundance of oxygen in the bulk Solar System, only C and H have high enough abundance to have significant effects on the oxygen fugacity. This study tunes the C abundance to adjust oxygen fugacity. The relationship between C/O and oxygen fugacity was shown in Grossman et al. (2008). In addition, the surface-energy barrier prevents the equilibrium between gas and solid from being achieved in a short time, so the partition between gas and solid is controlled by the kinetic process, rather than by chemical equilibrium. Therefore, a chemical equilibrium is established only among the gaseous phase of C, H, O, and refractory siderophile metals. The fugacity of the monatomic gases is derived from the equilibrium and will be used for the nucleation and condensation calculation in other modules.

2.2. Nucleation

The homogeneous nucleation theory (Becker and Döring, 1935) explains how the nucleation rate can be related with equilibrium state and gas-collision rate. The expression of the nucleation rate J is followed:

$$J = \left[\frac{1}{D_1^+ N_1} + \sum_{i=2}^{\infty} \frac{1}{D_i^+ N_{i,eq}} \right]^{-1} \tag{1}$$

where the D_i^+ is gas-collision rate between species i and its monomer, N_1 is number density of monomer, $N_{i,\ eq}$ is equilibrium number density of species i, k is Boltzmann constant, and T is temperature. The equilibrium number density can be obtained from the Gibbs free energy of formation.

$$N_{i,eq} \Big/ N_{\mathrm{std}} = \left(N_{1,eq} / N_{std} \right)^{n_i} exp\left(-\frac{\mu_i^0 - \sum \mu_1^0}{kT} \right) \tag{2}$$

where N_{std} is defined as $\frac{1\,\mathrm{bar}}{kT}$; μ_i^0 and μ_1^0 are the standard chemical potential of species i and its monomer, respectively. The question becomes
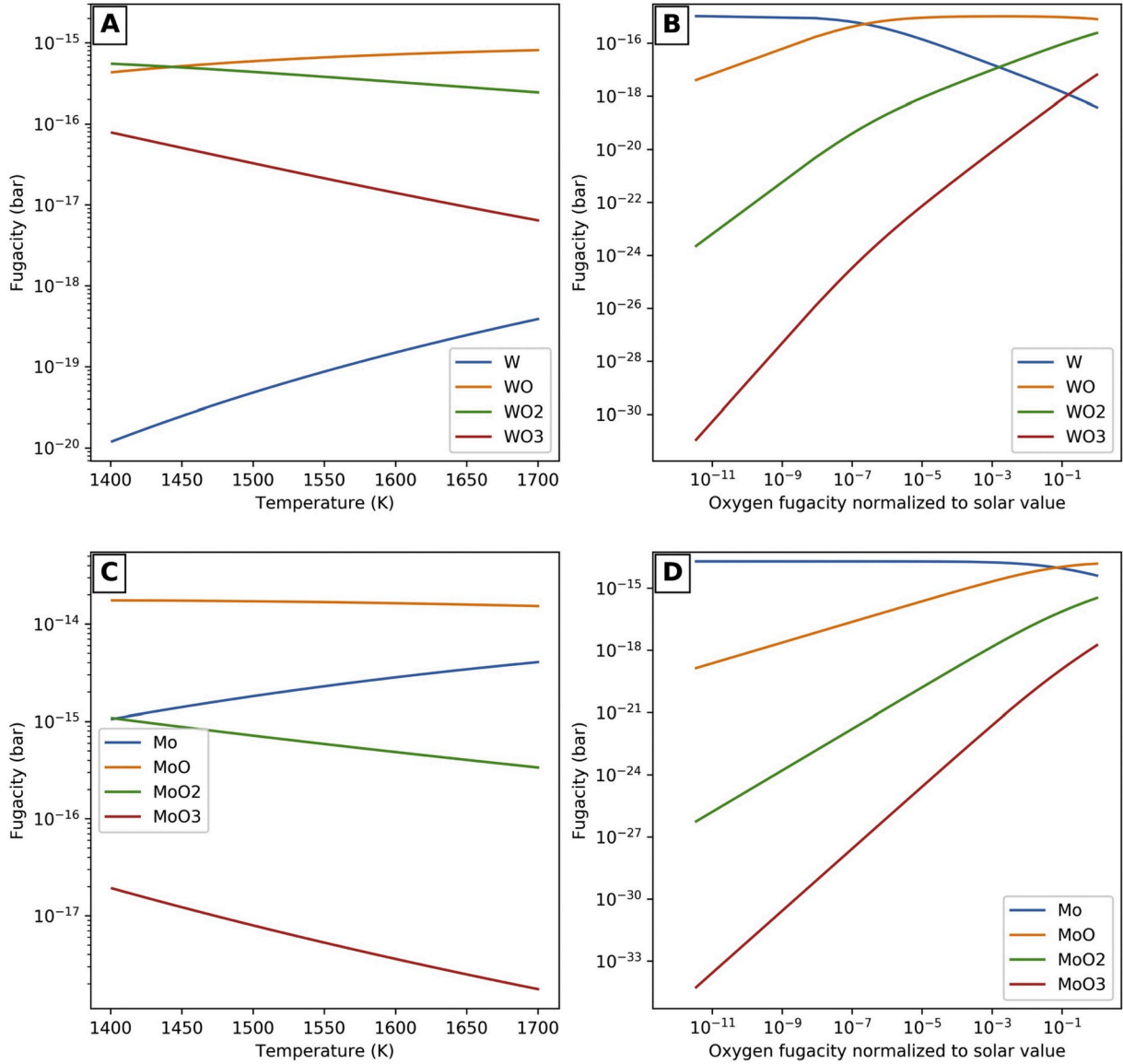
Fig. 2. Fugacity of gaseous species reaching equilibrium. The shown scenarios have total pressure of 10^{-4} bar. (A) Fugacity of W-bearing gases vs. temperature, where the oxygen fugacity is solar value. (B) Fugacity of W-bearing gases vs. oxygen fugacity, where the temperature is 1700 K. (C) Fugacity of Mo-bearing gases vs. temperature, where the oxygen fugacity is solar value. (B) Fugacity of Mo-bearing gases vs. oxygen fugacity, where the temperature is 1700 K.

to calculate D_i^+ and μ_i^0. The collision rate is straightforward, which can be calculated from the gas collision theory as followed:

$$D_i^+ = \pi(r_i + r_1)^2 v_{rel} N_1 = \pi(r_i + r_1)^2 \sqrt{\frac{8kT}{\pi \mu_{mass}}} N_1 \qquad (3)$$

where the r_i, v_{rel}, μ_{mass} are the radius of species i, the relative speed between species i and its monomer, and the reduced mass, respectively. The Gibbs free energy of clusters can be calculated from a semi-phenomenological model proposed by Tanaka et al. (2002):

$$\mu_i = n_i \mu_s^0 + \left[-kTln\frac{p_{sat}}{p_{std}} + \sigma_s A_1 \left(n_i^{\frac{2}{3}} - 1 \right) + \xi \left(n_i^{\frac{1}{3}} - 1 \right) \right] \qquad (4)$$

where p_{sat}, σ_s, and A_1 are the saturated pressure of the solid phase, surface energy, and surface area of a monomer, respectively. The surface energy of metals was obtained by Tyson and Miller (1977), Vitos et al. (1998), and references therein. The surface energy at any temperatures can be interpolated from the surface energy at zero Kelvin and that at the melting points of metals (Tyson and Miller, 1977). The data of surface

energy are shown in Table S2, and more discussion on the surface energy is in the Supplemental Information S5. The parameter ξ was originally derived from the second virial coefficient of vapor (Dillmann and Meier, 1991, Laaksonen et al., 1994), and Tanaka et al. (2002) proved that it could be obtained from the chemical potential of a dimer μ_2^0.

2.3. Solid solution

The effect of solid solution needs to be considered in the nucleation and growing process. Most RMNs have been observed to have a hcp structure (Harries et al., 2012), but the pure phases of refractory siderophile metals are not all hcp structure. The slight variation of Gibbs free energy due to crystal structure is not considered in this study, and the Gibbs free energy of the most stable structure is used for simplicity. Since the nucleation rate is derived from the number density of clusters and collision (growth) rate, these two variables need to be redefined for solid solution. For a cluster with n_i particles, it could have multiple microstates with different composition. For instance, for a two-particle cluster comprising Fe and/or Ni, the possible microstates are Fe—Ni,

Fe—Fe, Ni—Ni. Therefore, the number density of a cluster should be the sum of those of its microstates. Now, I will define some variables to describe the microstates: vector $\boldsymbol{n} = (n_1, n_2, ..., n_m)$ and $\boldsymbol{X} = (X_1, X_2, ..., X_m)$, where vector $\boldsymbol{n}$ records the number of particles of species (elements/isotopes) in one microstate and vector $\boldsymbol{X}$ represents the molar fraction of species in one microstate. The relationship between $\boldsymbol{n}$ and $\boldsymbol{X}$ is:

$$X = \boldsymbol{n} \Big/ \sum n_i \tag{5}$$

The number density of a microstate with total particles of $\boldsymbol{n}$ can be calculated as:

$$\frac{N_{\boldsymbol{n},eq}}{N_{std}} = \prod_{j=1}^{m} \left(\frac{N_{1,j}}{N_{std}} \right)^{n_j} exp \left(-\frac{\sum_{j=1}^{m} \left[X_j \left(\mu_{n,j}^0 - kTlnX_j \right) - n_j \mu_{1,j}^0 \right]}{kT} \right) \tag{6}$$

where m is the number of species; $N_{n,j}$ and $\mu_{n,j}^0$ are the number density and standard Gibbs free energy of the cluster with number n of species j, respectively; X_j is the molar fraction of species j in the microstate. The collision rate is similar, which is the sum of the collision rate with different gaseous metal atoms.

$$D_{\boldsymbol{n}}^+ = \sum_{j=1}^{k} \pi \left(r_{\boldsymbol{n}} + r_{1,j} \right)^2 \sqrt{\frac{8kT}{\pi \mu_{mass}}} N_{1,j} \tag{7}$$

where $D_{\boldsymbol{n}}^+$ and $r_{\boldsymbol{n}}$ are the collision rate and radius of the cluster with microstate $\boldsymbol{n}$, respectively; $r_{1,j}$ is the radius of the monomer of species j, respectively.

In principle, a cluster could contain all the metal species. However, containing too much unsaturated metal would make the cluster unstable. For example, the saturation rate (gas pressure divided by vapor pressure) of Fe is below 1% at high temperature. If a stable cluster with 99 particles collides with a Fe gas particle and forms a cluster with 100 particles, its Fe fraction (1%) will be higher than the saturation rate of Fe ($< 1\%$). It would dissociate quickly and break down to its original form. Therefore, when calculating the total collision rate of a cluster, I only count the elements that are stable in the cluster. The unsaturated metal can still condense on a grain after nucleation, but not during the nucleation process.

2.4. Grain growth

The growth of a grain is controlled by both condensation and evaporation. They are quantified by the Hertz-Knudsen equation (e.g., Davis and Richter, 2014). The condensation rate $Z_{in,i}$ of species i and the evaporation rate of a pure phase $Z_{out,i}^0$ can be represented as:

$$Z_{in,i} = \frac{\alpha_i P_{gas,i}}{\sqrt{2\pi m_i kT}} \tag{8}$$

$$Z_{out,i}^0 = \frac{\beta_i P_{sat,i}}{\sqrt{2\pi m_i kT}} \tag{9}$$

where $P_{gas,i}$, $P_{sat,i}$, m_i, α_i, and β_i are the gas pressure, saturated pressure, mass, sticking coefficient, and evaporation coefficient of the species i, respectively. The sticking coefficient of metals is close to unity (Tachibana et al., 2011). Evaporation coefficient is a function of temperature and grain composition (Fedkin et al., 2006; Tachibana et al., 2011). Since no experiments have yet been conducted to measure the evaporation coefficients of RMNs, the evaporation coefficient is assumed to be unity as well. If the grain is treated as a solid solution, the evaporation rate of individual elements $Z_{out,i}$ is modified as:

$$Z_{out,i} = \gamma_i x_i Z_{out,i}^0 \tag{10}$$

where γ_i and x_i are the corresponding activity coefficient and molar fraction of individual species. The net flux per unit area of species i, labeled as J_i, is the deviation between the condensation and evaporation rate of species i:

$$J_i = Z_{in,i} - \gamma_i x_i Z_{out,i}^0 \tag{11}$$

The increment of species i through time Δt is computed from integration:

$$\Delta n_i = \int_{t_0}^{t_0 + \Delta t} J_i S dt \tag{12}$$

where S is the surface area of the grain. The solution to this equation is shown in the Supplemental Information S2.

2.5. Model parameters

NUCON simulates the condensation of the following elements: Os, Re, W, Ir, Mo, Ru, Pt, Fe, and Ni. H, O, C are also considered to control the oxygen fugacity. Their abundance in the Solar Nebula is acquired from Lodders et al. (2009). The thermodynamic data of their solid and gaseous phases are taken from the JANAF table (Chase et al., 1998) and CRC Handbook of Chemistry and Physics (Rumble, 2017). The surface energy of their solids is chosen from Vitos et al. (1998). The discussion and validation of the thermodynamic data and surface energy are presented in the Supplementary Information S3, S5.

2.6. Assumptions and limitations

This study assumes that (1) the RMN-forming region has the solar composition with adjustable carbon abundance to control oxygen fugacity; (2) RMNs remain interacting with the nebula gases through the whole condensation process; (3) RMNs are single crystals with homogeneous composition, based on the observation of Harries et al. (2012); (4) equilibrium isotopic fractionation among phases is not considered in this study, because this effect is negligible for anhydrous minerals in high temperature (Sharp, 2017). Therefore, some limitations exist in this study: (1) the result of this study cannot be directly used to predict the nature of the RMNs from circumstellar environments (e.g. Croat et al., 2013); and (2) fractional condensation is not modeled, because the introduction of the sequestration of RMNs per step will lead to too many variables.

3. Results

3.1. Convergence to equilibrium condensation

NUCON model uses a numerical approach to compute the growth of RMNs. One method to examine the approach is to evaluate if it can reproduce the result of equilibrium condensation given a very low cooling rate. Pan (2019) has succeeded to use NUCON to reproduce the equilibrium condensation of most refractory siderophile metals given a cooling rate of 1.5×10^{-3} K/year. Besides reproducing the same result, this study also provides the details on how refractory siderophile metals condense and RMN composition evolves given a cooling rate of 1.5×10^{-3} K/year and total pressure of 10^{-4} bar (Supplementary Information S6). The consistency between the modeling result and our understanding of equilibrium condensation validates the condensation calculation in the NUCON model.

3.2. An example of RMN formation

This section shows examples of RMN formation under the total pressure and oxygen fugacity of 10^{-4} bar and $1 \times f_{O_2, \odot}$, respectively. Here, $f_{O_2, \odot}$ represents the oxygen fugacity of the canonical solar nebula with the solar abundance (Lodders et al., 2009). Various cooling rates are used in these examples and they will be specified later. The

formation of RMN is divided into two stages: (1) refractory-siderophile-metal condensation stage and (2) Fe—Ni condensation stage. A transition from the first to second stage occurs when Ni starts to saturate, which is set to be the time when the saturation ratio of Ni reaches 5% (1440 K with the total pressure of 10^{-4} bar). This criterion is used because most refractory siderophile metals have condensed at this point while Fe and Ni just start to condense (the molar fraction of Fe and Ni in RMN is <10%). Saturation ratio is defined as gaseous pressure p divided by the product of activity coefficient γ and vapor pressure p_{sat}, i.e. $\frac{p}{\gamma p_{sat}}$.

3.2.1. Refractory-siderophile-metal condensation

The process of refractory siderophile metal condensation is shown (Fig. 3). This cooling rate is set to be 0.15 K/year. The simulated nebula starts to cool down from 1844 K, where most refractory siderophile metals started to saturate. Due to the high surface energy of the refractory siderophile metals, no significant numbers of nuclei are generated. Supplementary Information S4 shows that the nucleation rate needs to reach 10^{-13} m^{-3}s^{-1} in order to generate significant numbers of nuclei. At 1535 K, nuclei begin to be generated (Fig. 3B) when the nucleation rate reaches 10^{-13} m^{-3}s^{-1}. Since most elements
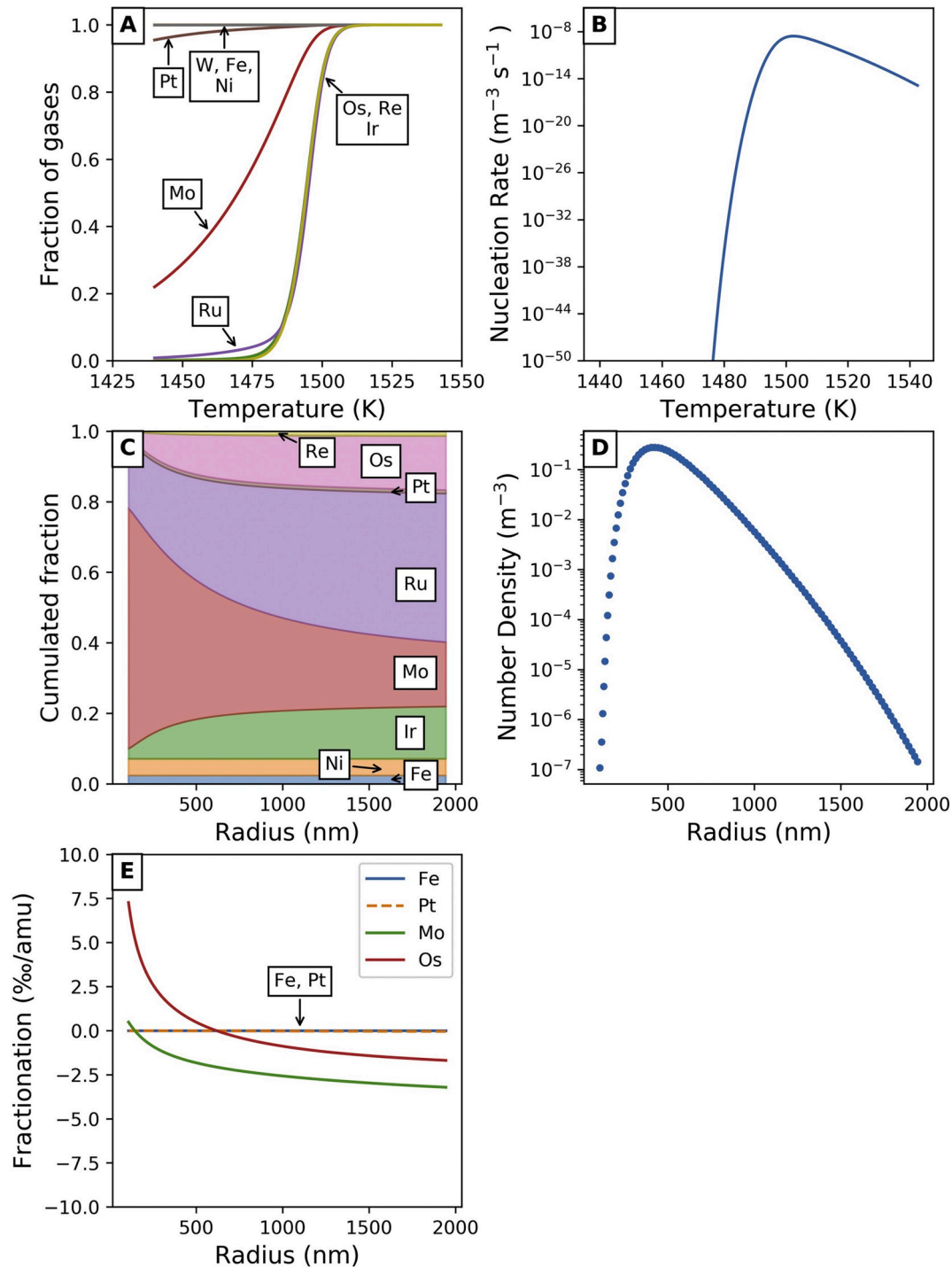

Fig. 3. The Result of refractory-siderophile-metal condensation with the pressure, oxygen fugacity, and cooling rate of 10^{-4} bar, $1 \times fO_{2, \odot}$, and 0.15 K/year, respectively. (A) The fraction of remaining gaseous molecules vs. temperature. (B) Nucleation rate vs. temperature. (C) The composition of the RMNs vs. radius at 1440 K. (D) Number density depending on the radius of the RMNs at 1440 K. (E) Isotopic fractionation of the RMNs depending on radius at 1440 K.

(Re, Os, W, Ir, Mo, Ru) have already extremely supersaturated, they begin to condense kinetically on the generated nuclei (Fig. 3A). From 1535 K to 1440 K, it takes <600 years to condense over 99% Re, Os, Ir, and Ru. Re, Os, Ir, and Ru have the same 50% condensation temperature, which is 1494 K. In the canonical solar nebula, only 10% of Mo exists as monatomic gas. Since the condensation rate is proportional to the fugacity of monatomic gas (Eq. (8)), the condensation of Mo is relatively slow (Fig. 2 for the fugacity of Mo). 50% Mo has condensed at 1470 K, and 80% Mo has condensed at 1440 K. W is much more oxidized than Mo, so W condenses extremely slowly and most W remains gaseous at this timescale. With the condensation of refractory siderophile metals, the nucleation rate finally decreases (Fig. 3B). Overall, given the kinetic inhibition of the nucleation, the RMN condensation at this condition deviates largely from the equilibrium process.

At the end of the refractory-siderophile-metal condensation stage, the radii of the RMNs range from 250 to 2000 nm, with the highest frequency at 500 nm (Fig. 3D). The RMNs forming earlier have larger radii. Elemental fractionation exists among RMNs: the larger grains are enriched in Os, Ir, and Ru, while the smaller ones are enriched in Mo (Fig. 3C). The isotopic fractionation of Os, Mo, Pt, and Fe are shown (Fig. 3E). The definition of isotopic fractionation is shown in Supplementary Information S7. From Os to Fe, the degree of isotopic fractionation increases with equilibrium condensation temperature decreasing. Given the supersaturation of Os and Mo, their isotopes are largely fractionated: larger RMNs are enriched in lighter isotopes while the smaller RMNs are enriched in heavy isotopes. Os (−2–5‰/amu) has more significant fractionation than Mo (−3–0.5‰/amu). The Pt and Fe of RMNs have no isotopic fractionation, indicating that they remain in equilibrium with Solar Nebula during condensation.

3.2.2. Fe—Ni condensation

The simulation transits from the stage of refractory-siderophile-metal condensation to Fe—Ni condensation stage when the saturation rate of Ni reaches 5% (see Section 3.2 for the reason). When the simulation enters the Fe—Ni condensation stage, only the cooling rate will be updated. This update tries to reproduce the scenario that RMNs may be transported from one forming region to another region with different cooling rates. The actual RMNs consist of Fe and Ni from <10 wt% to 90 wt% (e.g., Harries et al., 2012; Daly et al., 2017a). The simulation of Fe—Ni condensation continues to run until the RMNs contain Fe and Ni over 50 at.%, the average of the observed compositions shown above. Two examples on the Fe—Ni condensation stage with different cooling rates will be shown. They are run with the pressure and oxygen fugacity of 10^{-4} bar and $1 \times f_{O_2, \odot}$, respectively, following the refractory-siderophile-metal-condensation stage depicted above.

3.2.2.1. Slow cooling. The cooling rate is set to be 0.15 K/year, which is identical to the refractory-siderophile-metal condensation. The nebula continues to cool from 1440 K to 1363 K. At this slow cooling rate, the supersaturated Mo continues to condense kinetically, and it condenses
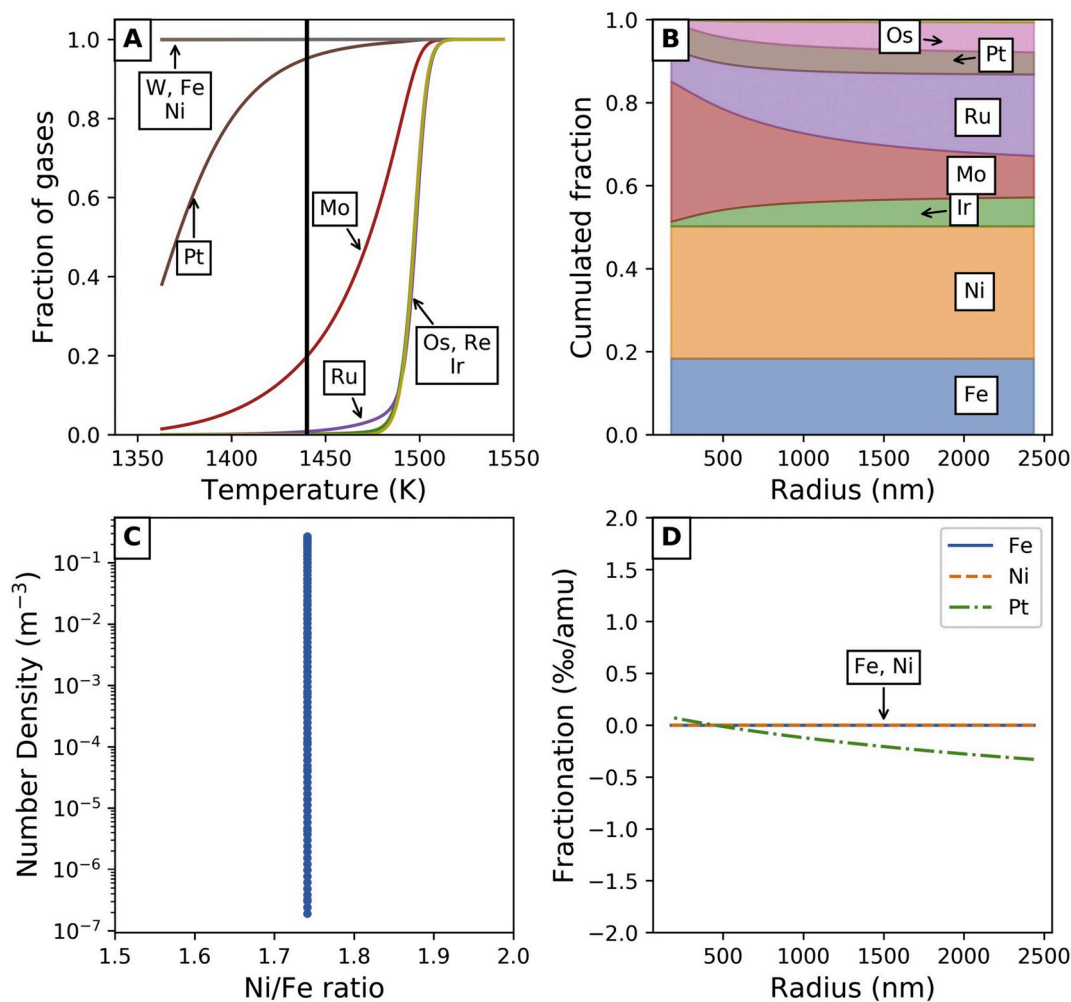

Fig. 4. The Result of Fe—Ni condensation with the pressure, oxygen fugacity, and cooling rate of 10^{-4} bar, $1 \times fO_{2, \odot}$, and 0.15 K/year, respectively. (A) The fraction of remaining gaseous species vs. temperature. (B) The composition of the RMNs vs. radius at 1363 K. (D) Number density depending on the Ni/Fe of the RMNs at 1363 K. (E) Isotopic fractionation of the RMNs depending on radius at 1363 K.

completely at around 1360 K (Fig. 4A). Pt also starts to condense significantly because it has reached saturation. Pt condenses in near equilibrium with the nebula gas, suggested by the weak mass-dependent isotopic fractionation of Pt (< 0.5‰/amu) (Fig. 4D). Most Fe and Ni remain in the nebula gas because the amount of Fe and Ni in RMNs is small compared to the bulk solar nebula (Fig. 4A). At 1363 K, the weak isotopic fractionation of Fe and Ni shows that they are in equilibrium with the nebula (Fig. 4D), so the Ni/Fe ratio of RMNs at 1363 K is the same as that from equilibrium condensation (Fig. S4). Despite the elemental fractionation of refractory siderophile metals, RMNs have uniform Fe and Ni composition (Fig. 4B).

3.2.2.2. Rapid cooling. In this example, the cooling rate is set to be 15 K/h. The system cools down from 1440 K to 1332 K. Given this rapid cooling, Fe—Ni condensation in this simulation lasts 6 h. It is too short for refractory siderophile metals to condense, so the abundance of Mo and Pt gases is "frozen". Most Fe and Ni remain in the nebula gas, like the slow-cooling case, because RMNs are small and only take a small amount of Fe and Ni (Fig. 5A). Fe and Ni quickly become supersaturated in this supercooling condition and condense kinetically. At 1332 K, the Ni/Fe ratio of RMNs ranges from 0.4 to 0.8 (Fig. 5C), which is deviated significantly from equilibrium value (about 1.5 from Fig. S4). The kinetic condensation of Fe and Ni is also reflected by their mass-dependent isotopic fractionation, whose value is around -2‰/amu and -5‰/

amu, respectively (Fig. 5D). Though Pt are also supersaturated, only a small amount of Pt has condensed on RMNs in this short timescale and the newly-condensed fractionated Pt cannot overprint the preexisting unfractionated Pt. Elemental fractionation exists among different sizes of RMNs: small grains tend to be enriched in Fe, Ni, and Mo, while large grains tend to have Os, Ir, and Ru. All RMNs are depleted in Pt and W (Fig. 5B).

3.3. Condensation temperature

This section explores how cooling rate, total pressure, and oxygen fugacity affect the condensation temperature of refractory siderophile metals. Here, condensation temperature of an element is defined as the temperature where 50% of the element condenses as solid. To acquire the condensation temperature at specific conditions, the program is run similarly as Section 3.2. However, instead of terminating the program when Fe and Ni start to saturate, the program will continue running until every refractory siderophile metal has condensed over 50%. The relationship between cooling rate and condensation temperature in five scenarios are shown (Fig. 6): the first three scenarios have solar oxygen fugacity ($1 \times f_{O_2, \odot}$), and total pressures of 10^{-3}, 10^{-4}, and 10^{-5} bar, respectively; last two scenarios have the total pressure of 10^{-4} bar, and oxygen fugacity are $10^{-4} \times f_{O_2, \odot}$ and $10^{-8} \times f_{O_2, \odot}$, respectively. All the figures include the equilibrium condensation temperature of elements
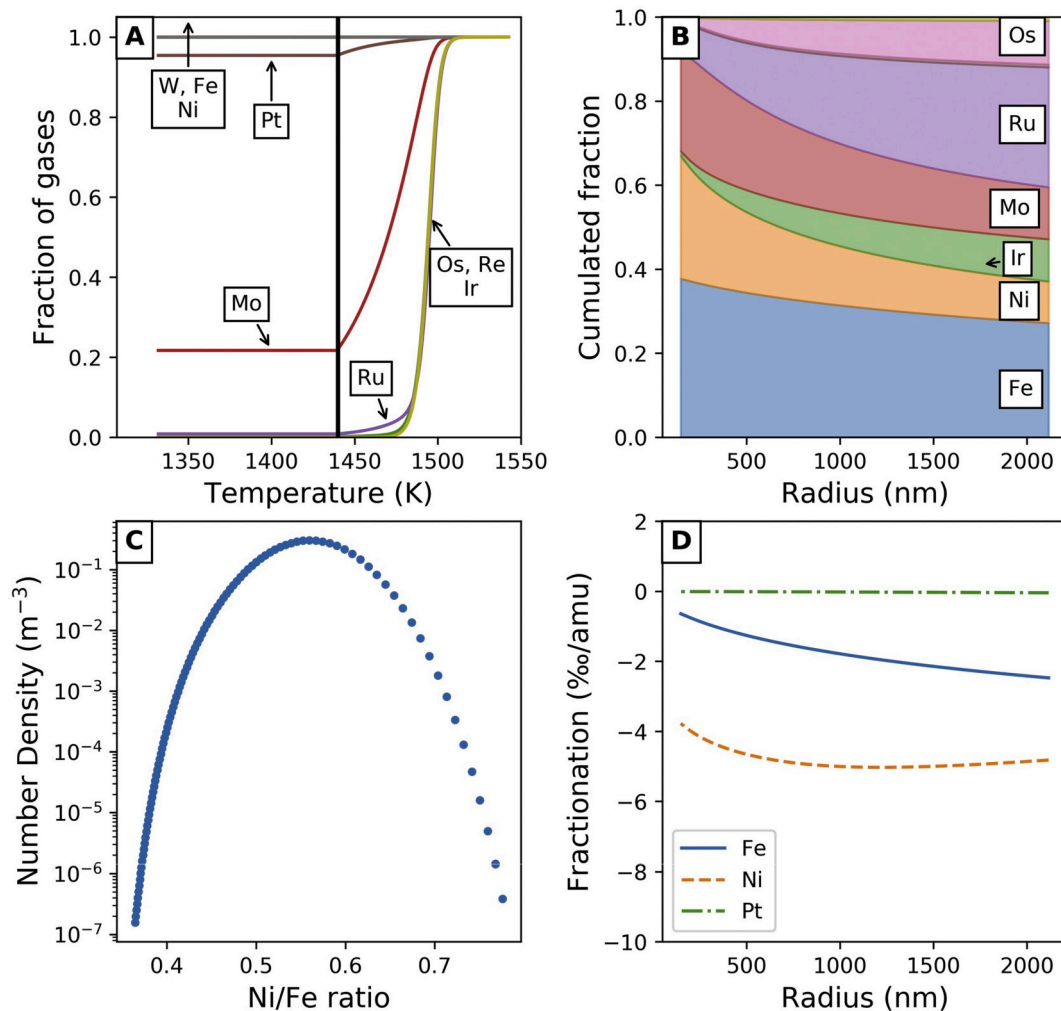

Fig. 5. The Result of Fe—Ni condensation with the pressure, oxygen fugacity, and cooling rate of 10^{-4} bar, $1 \times f_{O_2, \odot}$, and 15 K/h, respectively. (A) The fraction of remaining gaseous species vs. temperature. (B) The composition of the RMNs vs. radius at 1332 K. (D) Number density depending on the Ni/Fe of the RMNs at 1363 K. (E) Isotopic fractionation of the RMNs depending on radius at 1332 K.
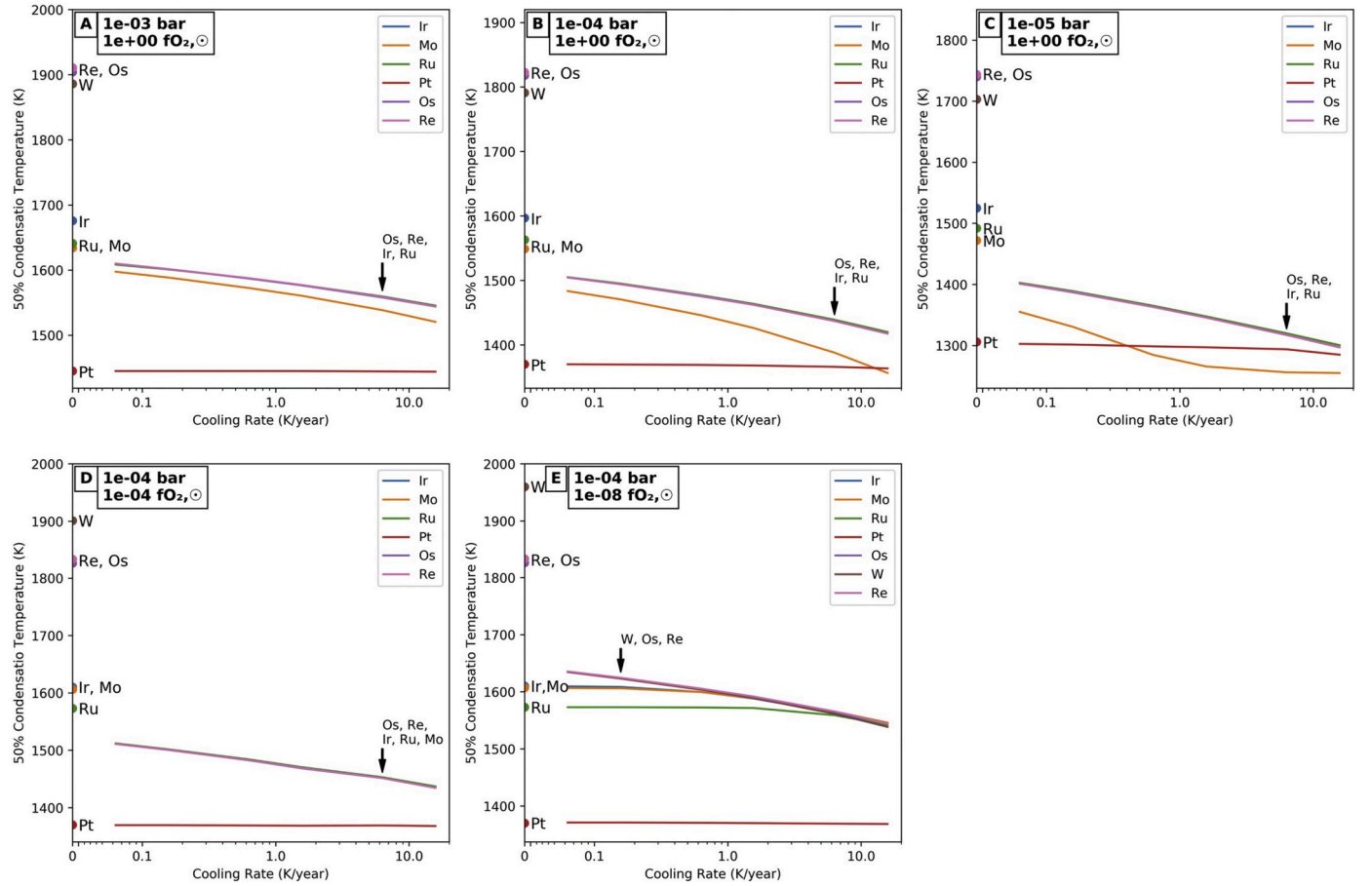
Fig. 6. The plots of 50% Condensation temperature vs. cooling rate. The environmental conditions are shown in each figure. The x-axis is scaled in logarithm from 0.05 to 20 K/year and linear from 0 to 0.05 K/year. Equilibrium condensation temperature is plotted on y-axis for reference.

for reference, which is plotted at y axis. All the results show that rapid cooling leads to lower condensation temperature. A large gap exists between equilibrium and kinetic condensation temperature, due to the kinetic inhibition of surface energy. The first three scenarios show higher pressure results in higher condensation temperature (Fig. 6A–C). All scenarios except the last one with the oxygen fugacity of $10^{-8} \times f_{O_2, \odot}$ indicate that Os, Re, and Ir condense simultaneously and have similar condensation temperature during kinetic condensation. The monatomic Mo and Ir have almost identical Gibbs free energy. However, at the solar oxygen fugacity, most gaseous Mo exists as oxide, and Mo condenses more slowly than Ir. Thus, Mo has lower condensation temperature than Ir. However, when the oxygen fugacity is lower than the canonical value (Fig. 6DE), where most Mo exists as monatomic gas, Mo and Ir condense in a similar way and have identical condensation temperature. Also, the equilibrium condensation temperature of Mo and W increases accordingly. At 10^{-5} bar and solar oxygen fugacity, the kinetic condensation temperature of Mo decreases with cooling rate. When cooling rate exceeds 2 K/year, the condensation temperature of Mo reaches 1270 K and begins to decrease mildly. The mild decrease is due to that Fe and Ni condense significantly below 1300 K and RMNs grow quickly, leading to larger surface area as well as faster condensation rate of Mo. At 10^{-4} bar and the oxygen fugacity of $10^{-8} \times f_{O_2, \odot}$, such reduced condition makes W the most refractory element and raises the condensation temperature of W. Os and Re condense together with W during kinetic condensation, because all of them are supersaturated. Since RMNs form at the temperature above the saturation of Mo, Ir, and Ru in this reduced condition, these three elements can condense in equilibrium at slow cooling rates. Thus, the condensation temperature of Ir, Mo and Ru converges to equilibrium condensation temperature when the cooling rate is below

1 K/year. When the total pressure is large enough (above 10^{-4} bar), the condensation temperature of Pt is almost constant to the equilibrium condensation temperature despite the cooling rate, which suggests that Pt is almost in equilibrium with the nebula even when the cooling rate is as high as 10 K/year.

3.4. RMN composition

To explore how total pressure and cooling rate affect RMN composition, the distribution of Mo/Os and Mo/Ru of RMNs are plotted (Fig. 7). These values represent the composition at the end of the refractory-siderophile-metal condensation stage (Section 3.2.1). Mo has lower condensation temperature than Os, so Mo/Os indicates whether a RMN is nucleated at the early or late stage of refractory-siderophile-metal condensation. Mo and Ru have similar condensation temperature in equilibrium, but Mo condenses more slowly than Ru due to partial oxidation of Mo atom. Hence, Mo and Ru could behave differently in different scenarios. Section 3.2.1 shows that Os and Ru condense simultaneously in the early stage of refractory-siderophile-metal condensation. Given this principle, the early-formed RMNs acquire solar Os/Ru ratio (Os/Ru is represented by the slope in the graph), despite the cooling rate and total pressure. Mo/Ru of late-formed RMNs varies based on the conditions, and it is positively related with cooling rate and negatively related with pressure. Among the RMNs from the same condensation process, the composition of the RMNs with highest number density (marked as circles) is used to represent the mean composition. The mean composition of RMNs is close to solar composition, except those forming at high cooling rate and low pressure. RMNs forming in rapid cooling are extremely depleted in Mo, indicating Mo
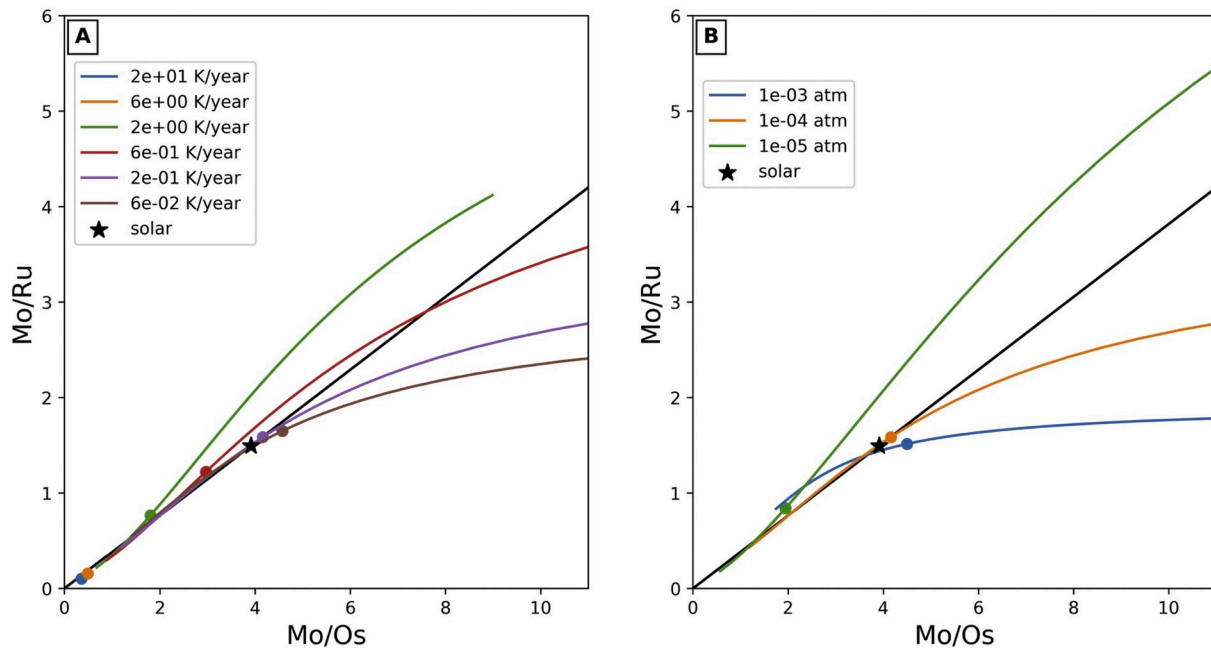
Fig. 7. (A) Mo/Ru vs. Mo/Os of RMNs condensing at different cooling rates. (B) Mo/Ru vs. Mo/Os of RMNs condensing at total pressures. The curves represent the distribution of RMNs. The circles represent the composition of the RMNs with highest number density, which is used to represent the mean composition of the RMNs forming in the same condition. The black line represents the solar Os/Ru.

has hardly condensed even when Fe and Ni become saturated.

3.5. Results of refractory-siderophile-metal condensation

This section shows how total pressure, oxygen fugacity and cooling rate affect the properties of RMNs. This study aims to find a robust indicator for the cooling rate of RMN-forming regions. Analogous to crystallization from magma, minerals form with small grain sizes during rapid cooling while they form with large grain sizes during slow cooling. Therefore, the radius of an RMN could reflect the cooling condition of condensation. In reality, the radii of RMNs may be hard to compare with one another due to the existence of Fe and Ni. Even two RMNs are formed in the same condition during refractory-siderophile-metal condensation; if one acquires more Fe and Ni before being captured by the host, it will have a larger radius than another. Therefore, "reduced radius" is introduced to make the comparison despite the dilution effect from Fe and Ni condensation. The reduced radius r_{red} is defined as the radius of an RMN whose Fe and Ni are removed,

$$r_{red} = r \, M_{RM}{}^{1/3} \tag{13}$$

where r and M_{RM} are the actual radius and molar fraction of refractory siderophile metals, respectively. This definition assumes all atoms have identical molar volume, and metallic atoms indeed share similar molar volume. Here is an example to compute the reduced radius: if an RMN has a radius of 500 nm and contains 80 mol% refractory siderophile metals, the reduced radius will be $500(0.8)^{1/3}$ nm, i.e. 464 nm. Section 3.2 shows that the RMNs forming in the same process can have various radii. It is helpful to calculate a metric to represent all the RMNs from the same process, and the mean reduced radius will be used here to study how the condensation conditions could impact the radii of RMNs. To obtain the mean reduced radius, the reduced radii of individual RMNs are computed first and then a weighted average of the reduced radii is calculated as the mean reduced radius, where the weight is the number density of RMNs.

When the total pressure is fixed, for example at 10^{-4} bar, the mean reduced radius of RMNs are plotted against cooling rate at various oxygen fugacities (Fig. 8A). The logarithm of the mean reduced radius of

an RMN decreases linearly with the logarithm of cooling rate, so regression lines are fitted for the mean reduced radius and cooling rate at log scale. Given the same cooling rate, for example at 0.06 K/year, the mean reduced radius varies from 600 nm to 1500 nm with different oxygen fugacities, but this variation is negligible in terms of log scale. Therefore, oxygen fugacity has limited effect on the mean reduced radius of RMNs, because the regression lines of different oxygen fugacities almost overlap.

When the oxygen fugacity is fixed, i.e., at $1 \times f_{O_2, \odot}$, the logarithm of mean reduced radius of RMNs are plotted against the logarithm of cooling rate at different pressures. Since the logarithm of reduced radius and cooling rate shows a linear relationship, their regression lines are plotted as well (Fig. 8B). Higher total pressure generates RMNs with larger grain sizes. Given the cooling rate of 1 K/year, the reduced radius increases from 20 to 2000 nm when the total pressure increases from 10^{-5} to 10^{-3} bar. The slopes of the regression lines between the logarithm of the reduced radius of an RMN and cooling rate show that the reduced radius is very sensitive to the cooling rate. Increasing cooling rate would result in smaller grain size. If the total pressure and oxygen fugacity are 10^{-4} bar and $1 \times f_{O_2, \odot}$, respectively, the reduced radius increases from 20 nm to 1000 nm when the cooling rate decreases from 10 K/year to 0.1 K/year.

3.6. Results of Fe—Ni condensation

The kinetic condensations of Fe and Ni on RMNs can result in unique Fe and Ni composition. The mean Ni/Fe ratio and isotopic fractionation of the RMNs from the same condensation process are evaluated here to explore their relationship with pressure, oxygen fugacity, and cooling rate during Fe—Ni condensation. NUCON simulates multiple scenarios with the oxygen fugacities between $10^{-8} \times f_{O_2, \odot}$ and $1 \times f_{O_2, \odot}$, total pressure from 10^{-5} to 10^{-3} bar, and cooling rate of Fe—Ni condensation stage from 0.2 K/h to 200 K/h.

The results are shown at Fig. 9. When the total pressure is fixed, e.g., at 10^{-4} bar, the mean Ni/Fe ratio and the isotopic fractionation of Fe and Ni are plotted against cooling rate with various oxygen fugacities. Curves corresponding to different oxygen fugacities overlap with one another (Fig. 9ACE), indicating that the redox condition contributes
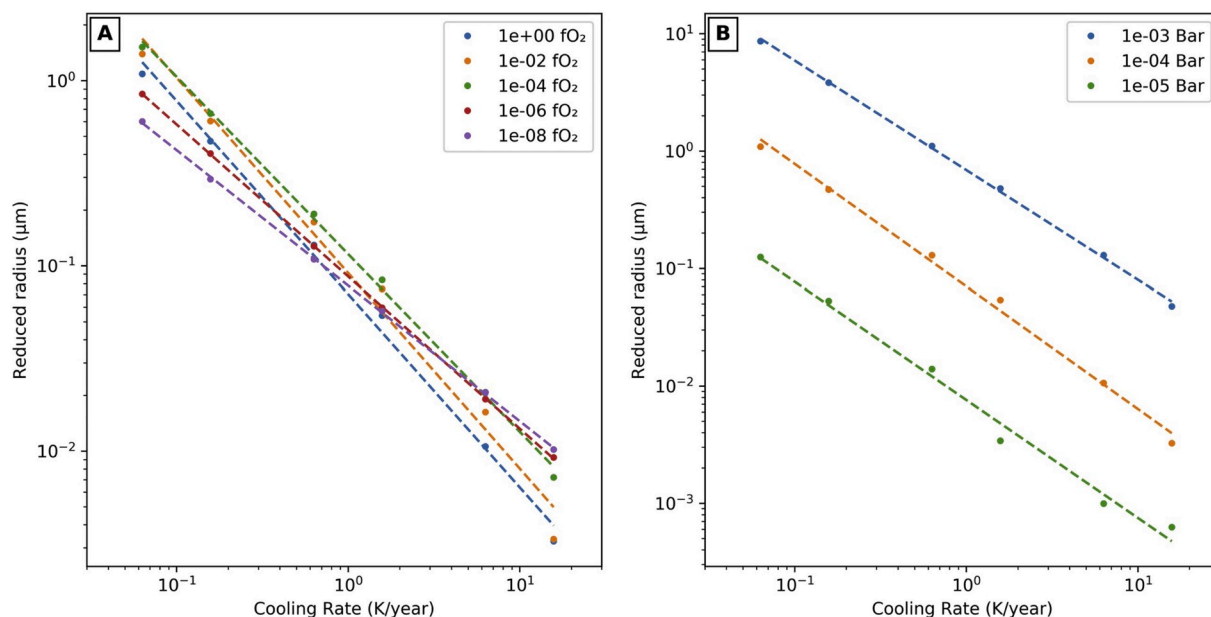
Fig. 8. Log-log plots of the reduced radius of RMN and cooling rates during refractory-siderophile-metal condensation. (A) The data are generated with the total pressure of 10^{-4} bar and oxygen fugacities from $10^{-8} \times f_{O_2, \odot}$ to $1 \times f_{O_2, \odot}$. Regression lines are fitted for the data grouped by oxygen fugacity. (B) The data are generated with the oxygen fugacity of $1 \times f_{O_2, \odot}$ and pressure from 10^{-5} to 10^{-3} bar.

little to the Ni/Fe ratio and isotopic fractionation. Since the oxygen fugacity of the Solar Nebula was far below the Fe-FeO and Ni-NiO oxygen buffers (Grossman et al., 2008), both the Fe and Ni gases exist as monatomic gases, so the oxygen fugacity should have little effect on their condensation. The slight variation among the curves of different oxygen fugacities should result from other properties of RMNs, like the radii of RMNs, which are slightly affected by oxygen fugacity (Fig. 8A). When the total pressure varies from 10^{-5} to 10^{-3} bar, the curves of the mean Ni/Fe ratio and Fe, Ni isotopic fractionation still overlap, which means that the total pressure also has little effect on the mean Ni/Fe ratio and Fe, Ni isotopic fractionation of RMNs. (Fig. 9BDF).

However, the mean Ni/Fe ratio and Fe, Ni isotopic fractionation are sensitive to cooling rate. Higher cooling rate would result in lower Ni/Fe ratio and larger isotopic fractionation (Fig. 9). When the cooling rate is lower than 0.02 K/h, the Ni/Fe ratio gradually converges to the equilibrium value. The Fe and Ni isotopic fractionation are also close to zero. When the cooling rate is above 50 K/h, the Ni/Fe ratio is below 0.2. Both the Fe and Ni fractionation are lower than −5‰/amu. While Fe isotopic fractionation monotonically decreases with cooling rate, Ni isotopic fractionation decreases in the beginning and then slightly increases again. It can be explained by the mixing between preexisting unfractionated Ni and newly-condensed fractionated Ni: the RMNs are set to accumulate Fe and Ni until the RMNs contain 50% Fe and Ni. At rapid cooling, both Fe and Ni are supersaturated and Fe condenses much faster than Ni, so the newly-condensed material on RMNs mainly consists of Fe (i.e. low Ni/Fe ratio). Thus, though newly-condensed Ni is highly fractionated, less Ni has condensed during rapid cooling than that during slow cooling, so less fractionated Ni overprints the unfractionated Ni. Nevertheless, both the mean Ni/Fe ratio and Fe isotopic fractionation are monotonic functions of the cooling rate, and can be regarded as potential indicators for the cooling rate during Fe—Ni condensation.

4. Discussion

4.1. Review of condensation origin of RMNs in literature

The modeling results (Sections 3.5 and 3.6) indicate that both the mean reduced radius and Ni/Fe ratio of RMNs can be used to infer the cooling rate of RMN condensation. However, Schwander et al. (2015a) shows that not every RMN formed through condensation, and those in molten CAIs likely precipitated from CAI melts, so it is necessary to examine the origin of RMNs. Published papers have detailed characterization of RMNs in the CAIs, but some of them lack the information of their origin, leaving the possibility that they might not condense from the Solar Nebula. Wark and Lovering (1976) were the first ones to discover RMNs in a Type A CAI and claimed the CAI might have been formed by condensation. Palme et al. (1982) characterized 7 RMNs from an ultra-refractory CAI, which could either be the first condensate or an evaporation residue. Wark (1986) found a few RMNs in a CAI condensing through multi stages. Berg et al. (2009) and Harries et al. (2012) extracted RMNs from acid residue, so the host phases are unknown. Schwander et al. (2015a) observed most of their RMNs in compact CAIs, which likely formed from liquid or experienced re-melting. Therefore, the RMNs there should have formed by precipitating from CAI melt, rather than gas-solid condensation. Daly et al. (2017a) used Synchrotron X-ray Fluorescence (SXRF) and discovered a large number of RMNs. They claimed that some of the compositional variety among the analyzed RMNs may be inherited from the presolar molecular cloud, which could be a mixture of circumstellar environments. However, the compositional variety alone is not enough to support a condensation origin, because the RMNs could have precipitated from early-formed CAIs that inherited the molecular cloud composition. Daly et al. (2017a) discovered some of the host CAIs were unmolten, suggesting that the included RMNs could have the condensation origin. Daly et al. (2017b) discovered some RMNs in a fluffy type A inclusion, whose backscattered electron (BSE) image showed it did not experience melting. Fischer-Gödde et al. (2018) discovered that RMNs from the Allende meteorite displayed distinctive Ru isotopic anomaly from the CAIs of Allende. Since the RMNs were extracted from the acid residue of Allende, it is impossible to identify the host of these RMNs. Also, the radius and Ni/Fe ratio of these RMNs are not provided. Given the above information, it seems that the RMNs from Wark and Lovering (1976), Wark (1986), Daly et al. (2017b), and some from Daly et al. (2017a) were confirmed to have condensation origin and their radii and composition were measured. Nevertheless, in the following discussion I will take into account the RMNs from the literature mentioned above except Schwander et al. (2015a). The reduced radius and Ni/Fe ratio of the RMNs in literature are plotted in Figs. 10 and 11, respectively. Most
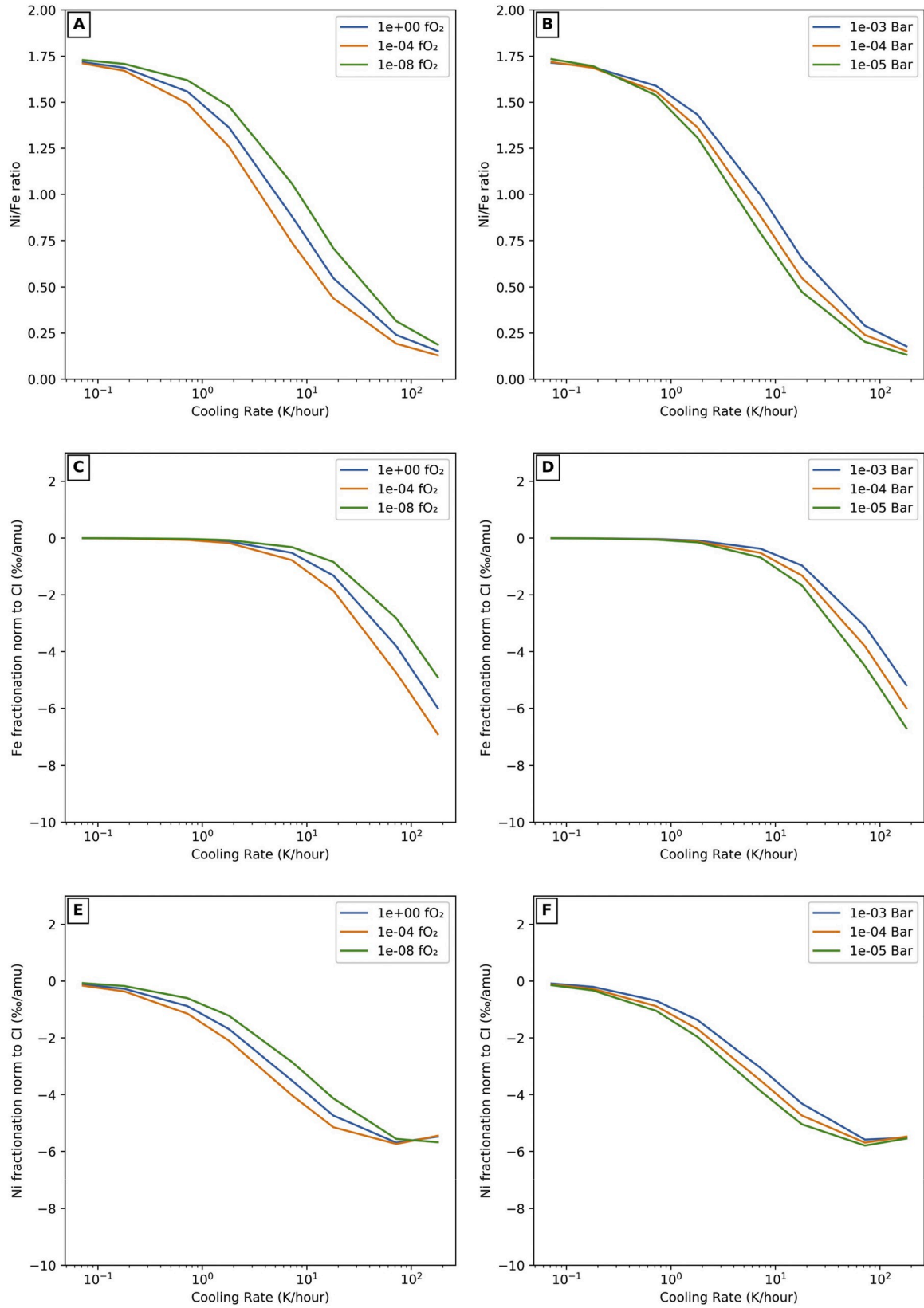
Fig. 9. (AB) The mean Ni/Fe ratio of the RMNs from the same condensation process vs. cooling rate during Fe—Ni condensation. (CD) The mean Fe isotopic fractionation normalized to the Solar Nebula vs. cooling rate during Fe—Ni condensation. (EF) The mean Ni isotopic fractionation normalized to the Solar Nebula vs. cooling rate during Fe—Ni condensation. (ACE) The data are generated with the total pressure of 10^{-4} bar and oxygen fugacities from $10^{-8} \times f_{O_2, \odot}$ to $1 \times f_{O_2, \odot}$. (BDF) The data are generated with the oxygen fugacity of $1 \times f_{O_2, \odot}$ and pressure from 10^{-5} to 10^{-3} bar.

RMNs have reduced radii between 100 nm – 1000 nm. Their Ni/Fe ratios range from 0 to 1.5, most of which are located between 0 and 1.0.

4.2. Prediction model of cooling rates based on RMNs

Sections 3.5 and 3.6 show that the cooling rate can be inferred from mean reduced radius and Ni/Fe of the RMNs, if the total pressure and oxygen fugacity of the forming environment are assumed. One difficulty of this inference is to select a collection of RMNs with the same origin. It is possible that RMNs in the same CAI might have the same origin, but evidence like isotopes is needed to support this possibility. Also, most RMN data do not include their location. Thus, it is hard to group the RMNs in literature by their forming region. This study assumes that the observed properties of individual RMNs represent the mean property of the RMNs from the same condensation process, and individual RMNs are used to infer the cooling rate. This assumption will increase uncertainty: the deviation of the reduced radius of individual RMNs and their mean reduced radius can vary in a factor of 3 (Fig. 3D) and the deviation of Ni/Fe can vary around 0.2 (Fig. 5C). Further discussion on calibrating the uncertainty is presented in Section 4.5. Another assumption in this study is that the forming region of RMNs had the solar abundance. The inference of cooling rate would fail if the forming region inherited the circumstellar environment or significant isolation of RMNs happened during condensation.

Based on the above assumptions, the reduced radius of an RMN is used to infer the cooling rate during refractory-siderophile-metal condensation. Section 3.5 shows the reduced radius is not sensitive to the oxygen fugacity. Only the total pressure needs to be considered as an additional variable. However, there is no effective cosmochemical barometer, so the total pressure is assumed to range from 10^{-5} to 10^{-3} bar. Here a regression model is fitted by the reduced radii of RMNs at various pressures. The reduced radii grouped by pressure are used to fit the regression, despite their oxygen fugacity. The log-log plots of the reduced radius of an RMN and cooling rate (Fig. 8) have shown an obvious linear relationship, so a regression function is set up as follows:

$$lnC = klnr + b \tag{14}$$

Fig. 11. Histogram of Ni/Fe ratios of RMNs from the literature (Wark and Lovering, 1976; Palme et al., 1982; Wark, 1986; Berg et al., 2009; Harries et al., 2012; Daly et al., 2017a, 2017b). The orange vertical line marks the solar Ni/Fe ratio.

$$C = e^b r^k \tag{15}$$

where r and C are reduced radius and cooling rate during refractory-siderophile-metal condensation, respectively; k and b are the parameters to be fitted. The fitted values are shown in (Table 1). The regression lines with prediction intervals are shown in Fig. S5. The uncertainty of cooling rate is about a factor of 2, and the prediction intervals of the regressions with different pressures do not overlap, suggesting that total pressure indeed plays an important role to infer cooling rates.

The Ni/Fe ratio of an RMN is used to infer cooling rate during Fe—Ni condensation. Section 3.6 shows the Ni/Fe ratio is insensitive to both pressure and oxygen fugacity and is a monotonic function of cooling rate. However, Ni/Fe ratio and cooling rate are not linearly correlated in any forms. When the cooling rate is low, the ratio is close to the value from equilibrium condensation. When the cooling rate is high, it converges to the solar Ni/Fe ratio as their condensation rates are proportional to their partial pressures (Eq. (8)). To fit this pattern, a sigmoid function is used in the following form:
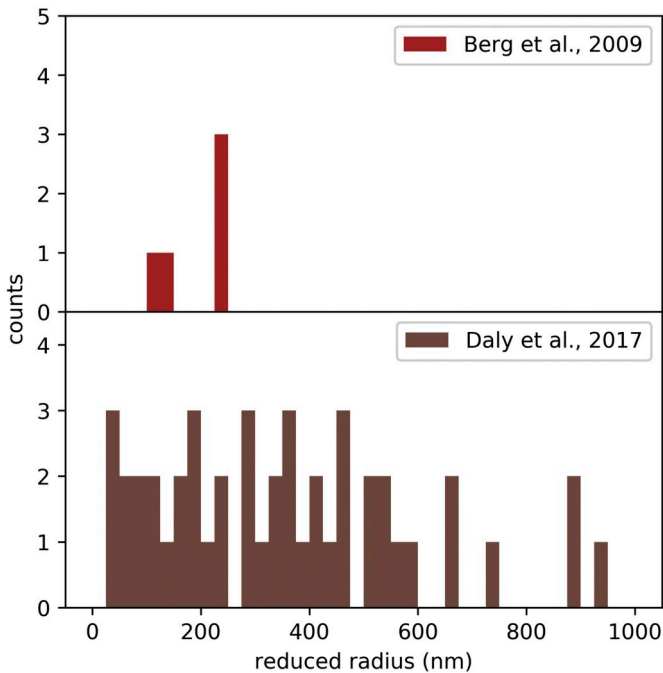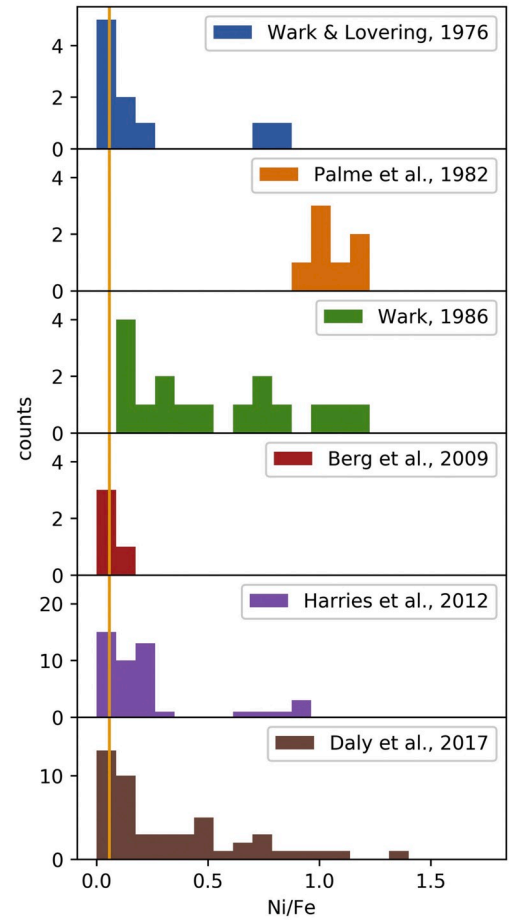

Fig. 10. Histogram of the reduced radii (defined in the Section 4.3) of RMMs from the literature (Berg et al., 2009; Daly et al., 2017a, 2017b).

Table 1
The parameters of regression between the mean reduced radius of RMNs and cooling rate during refractory-siderophile-metal condensation (Eq. (15)).

Pressure	k	b
10^{-3} bar	−0.8505	−14.093
10^{-4} bar	−0.8589	−16.041
10^{-5} bar	−0.8484	−18.025

$$R = \frac{a}{1 + bexp(clnC)} + [\text{Ni/Fe}]_\odot \qquad (16)$$

where R and C are Ni/Fe ratio and cooling rate during Fe—Ni condensation, respectively. a, b, and c are the parameters to be fitted. [Ni/Fe]$_\odot$ represents the solar Ni/Fe ratio, which is around 0.0556 (Lodders et al., 2009). The fitted values are shown in Table 2. The fitted curve is shown in Fig. S6. To be noticed, the inferred cooling rate is very sensitive to Ni/Fe when Ni/Fe is higher than 1.7. Slight variation by 0.1 in Ni/Fe can result in significant variation in cooling rate by over an order of magnitude. Since the assumption to use individual RMNs to represent a group of RMNs could lead to an uncertainty of 0.2 in Ni/Fe, the predicted cooling rate could be inaccurate when the measured Ni/Fe is over 1.7. Similarly, when the Ni/Fe ratio is below 0.2, the inferred cooling rate could also be inaccurate. Therefore, an effective bound is set for this prediction model: only when Ni/Fe is between 0.2 and 1.7 can the model predict a confident cooling rate. If the Ni/Fe ratio is higher than 1.7, the model could only confidently infer that the cooling rate is lower than 0.1 K/h. Similarly, if Ni/Fe is below 0.2, the cooling rate could only be inferred to be higher than 100 K/ h. In addition to cooling rate, the variation of Ni/Fe due to pressure and oxygen fugacity is relatively small, so the uncertainty introduced by them is not considered.

In principle, regression can also be generated for Fe, Ni isotopic fractionation. Since no mass-dependent fractionation of Fe and Ni has ever been measured for RMNs by any literature, no inference can be placed for cooling rate from the Fe, Ni isotopes. Their regression and discussion are shown in Supplementary Information S7.

The radii and composition of the RMNs in literature are converted to reduced radii and Ni/Fe ratios, which are put into the regression models to infer the cooling rates. One caveat should be mentioned again: the reduced radius should only infer the cooling rate during condensation of refractory siderophile metals (e.g. around 1500 K given the 10^{-4} bar and solar oxygen fugacity), while the Ni/Fe ratio should infer the cooling rate during Fe—Ni condensation (e.g. below 1400 K at 10^{-4} bar).

4.3. Inferred cooling rates during refractory-siderophile-metal condensation

Only four studies mentioned above (Wark and Lovering, 1976; Berg et al., 2009; Daly et al., 2017ab) provide the radii of RMNs, which are used to infer cooling rates during refractory-siderophile-metal condensation (Fig. 12). Wark and Lovering (1976) only provided the range of the diameters (500–3000 nm), so a segment instead of points is plotted to present cooling rates. The inferred cooling rates during refractory-siderophile-metal condensation vary with the assumed total pressure. When total pressure increases by a factor of 10, the inferred cooling rate will increase approximately by a factor of 10 as well. Even with the total pressure as high as 10^{-3} bar, the cooling rate during the refractory-siderophile-metal condensation was inferred to be lower than 30 K/ year. This upper bound is supported by the smallest grain in the studied RMNs with the reduced radius of 45 nm. Despite the assumed total pressure, the RMNs from different studies indicate a similar range of cooling rates during refractory-siderophile-metal condensation, which is between 10^{-2} and 10 K/year at 10^{-4} bar. The RMNs from Wark and Lovering (1976) indicate a range of cooling rates from 0.1 to 0.4 K/year. The RMNs from Berg et al. (2009) yield slightly higher cooling rates,

Table 2
The parameters of regression between the mean Ni/Fe ratio of RMNs and cooling rate during Fe—Ni condensation (Eq. (16)). The last row represents the parameters fitted by all the Ni/Fe data despite pressure.

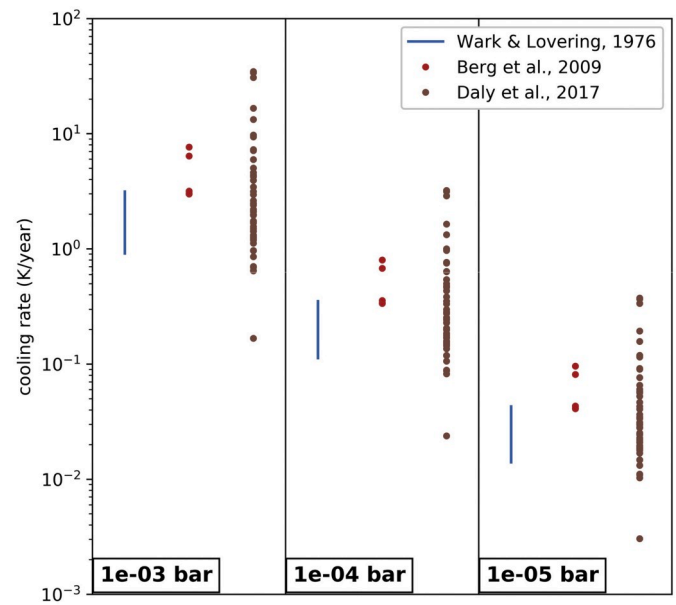| Pressure	a	b	c
10^{-3} bar	1.6826	0.1336	0.8966
10^{-4} bar	1.6947	0.1758	0.8887
10^{-5} bar	1.7134	0.2164	0.9174
–	1.6966	0.1755	0.8905

Fig. 12. Prediction of cooling rate during refractory-siderophile-metal condensation from the reduced radii of RMNs in the literature. Prediction is made separately for the total pressure from 10^{-5} to 10^{-3} bar.

which are between 0.2 and 1 K/year. This range is consistent with their study, which estimates a cooling rate of 0.5 K/year. The CAI-host RMNs from Daly et al. (2017a, 2017b) contain varieties of reduced radii from 45 to 3600 nm, so the inferred cooling rate cover a large range from 0.01 to 30 K/year.

4.4. Inferred cooling rates during Fe—Ni condensation

When it comes to the Ni/Fe ratio, more studies (Wark and Lovering, 1976; Palme et al., 1982; Wark, 1986; Berg et al., 2009; Harries et al., 2012; Daly et al., 2017a, 2017b) are used to infer the cooling rate during Fe—Ni condensation. Their Ni/Fe ratios range from 0 to 1.5. However, the regression method only works for a certain range of Ni/Fe ratios. Condensation, despite kinetic or equilibrium, can only generate RMNs with the Ni/Fe ratio between the equilibrium value (around 1.8 at 1400 K, Fig. S4) and the solar value (around 0.05). If an RMN has Ni/Fe ratio out of this range, it could not be explained by condensation from a canonical Solar Nebula. Instead it might condense from a fractionated nebula or circumstellar environment. It is also possible that the lab analysis on RMNs (e.g. acid treatment) might alter the composition of RMNs. For example, three RMNs from Berg et al. (2009) have Ni/Fe ratio of 0, which might result from condensing from a Ni-poor environment or being altered by acid treatment. Therefore, only the RMNs whose Ni/Fe is between solar and equilibrium value are used to infer cooling rate. In addition, the regression of Ni/Fe can only provide a lower bound for the inferred rapid cooling if Ni/Fe is near the solar value, and provide an upper bound for the cooling rate when Ni/Fe is near the equilibrium value (Section 4.2). The effective range of cooling rate is approximately between 0.1 and 100 K/h. For example, if a cooling rate is derived to be 500 K/h, it may not be accurate, but it is guaranteed to be larger than 100 K/h. The inferred cooling rates during Fe—Ni condensation are plotted in Fig. 13. The numbers of RMNs with the inferred cooling rate over 100 K/h are plotted as well. The RMNs from Wark and Lovering (1976), Wark (1986), Harries et al. (2012), and Daly et al. (2017a, 2017b) derive similar cooling rates from 1 K/h to over 100 K/h. The RMNs from Palme et al. (1982) indicate a narrow range of cooling rates between 1 and 2 K/h. Only one RMN from Berg et al. (2009) has Ni/Fe ratio between solar and equilibrium value, and derives a cooling rate over 100 K/h. All the RMNs predict that the cooling rate during Fe—Ni

condensation was above 1 K/h.

Experiments on CAI melts concluded that CAIs might have formed with cooling rate around 0.1–100 K/h (Stolper and Paque, 1986). A petrographic study on a CAI-AOA compound object also inferred a cooling rate of 50 K/h during CAI condensation (Komatsu et al., 2018). RMNs were likely captured by CAIs during Fe—Ni condensation, where they could significantly obtain Fe and Ni. The cooling rates inferred from Ni/Fe ratios should be able to be applied to the CAI-forming region. The Ni/Fe ratios of RMNs infer the cooling rate during Fe—Ni condensation from 2 K/h to over 100 K/h. Despite the RMNs in different literature infer different ranges of cooling rate during Fe—Ni condensation, they are more-or-less consistent with the cooling rate of the CAI-forming regions suggested by Stolper and Paque, 1986 and Komatsu et al. (2018). Given that CAIs were likely formed in the inner protoplanetary disk of the Solar System, whose distance to the Sun was <0.5 AU (Ireland and Fegley Jr, 2000; Woolum and Cassen, 1999), the cooling rates inferred from the literature and this study could together constrain the temperature evolution of the inner Solar System.

On the other hand, the cooling rate during refractory-siderophile-metal condensation is derived to be lower than 30 K/year for most RMNs, which is around 10,000 times lower than the cooling rate during Fe—Ni condensation. The difference in cooling rate indicates a two-stage condensation for RMN: (1) nucleation and growth of refractory siderophile metals in a slow-cooling region at high temperature, and (2) condensation of Fe and Ni in a rapid-cooling region at moderate temperature. Since the reduced radius and Ni/Fe ratio inferring for the slow and rapid cooling coexist in every individual RMNs, this dramatic transition of cooling rates could take place ubiquitously in the RMN-forming region.

4.5. RMN composition and cooling rate

The above inference assumes the composition of individual RMNs can represent the mean composition of the RMNs from the same condensation process. However, the composition of RMNs can deviate from the mean composition and their radii cannot represent the mean reduced radius. Inaccurate cooling rates during refractory-siderophile-metal condensation will thus be inferred based on the radii of these RMNs. If the radius of a lately-formed RMN is used to infer cooling rate, the cooling rate will be overestimated because it has a smaller radius
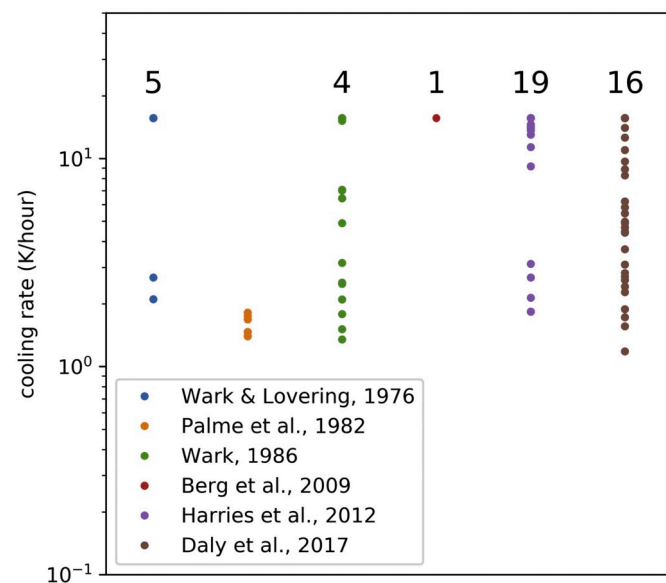
than the RMN with mean composition. Similarly, the inferred cooling rate from early-formed RMNs could be underestimated. Section 3.5 shows that early-formed RMNs are enriched in Os and Ru, while lately-formed RMNs are enriched in Mo. To evaluate how the composition could be used to calibrate the inferred cooing rate, Mo/Os and Mo/Ru of the RMNs in literature (e.g., Daly et al., 2017ab) are plotted along with the modeled RMN distributions (Fig. 14). The pressure is assumed to be 10^{-4} atm. Total pressure could have an impact on Mo/Ru, but it is obvious only on lately-formed RMNs (Fig. 7B). The composition of many RMNs are located around the solar composition and the mean composition of the RMNs forming under the cooling rate between 0.2 K/year and 2 K/year. If their inferred cooling rates also locate in this range, then their cooling rates likely reflect the actual value. Some RMNs (e.g. label 12–19 in Daly et al., 2017a) are extremely depleted in Mo, which are located near the origin. Their inferred cooling rates during refractory-siderophile-metal condensation range from 0.6 to 3 K/year given the pressure of 10^{-4} atm. Since none of them infer a rapid cooling rate over 6 K/year, the absence of Mo cannot be explained by rapid cooling. Instead, it is likely that these RMNs formed in the early stage of condensation, and their inferred cooling rates are underestimated. On the other hand, a few RMNs are located in the Mo-rich region, and their cooling rate could have been overestimated. Two RMNs (label 40, 101 in Daly et al., 2017a) are enriched in Mo but have undetectable Os: they could have formed in the very late stage of condensation, or they might have originated from a non-canonical Mo-rich nebula. One RMN (label 53 in Daly et al., 2017a) are enriched in Mo but has undetectable Ru and a few RMNs have neither detectable Os nor Ru. Their composition cannot be explained by the condensation from a canonical Solar Nebula, so their inferred cooling rate is invalid.

4.6. Condensation temperature

Tanaka et al. (2002) provided the condensation temperature of refractory siderophile metals at 10^{-5} bar and solar oxygen fugacity. Their cooling pattern was different from this study: they assumed that the

Fig. 13. Prediction of cooling rate during Fe—Ni condensation from the Ni/Fe ratios of RMNs in the literature. Numbers represent the amount of RMNs with the inferred cooling rate above 100 K/h or below 0.1 K/h.
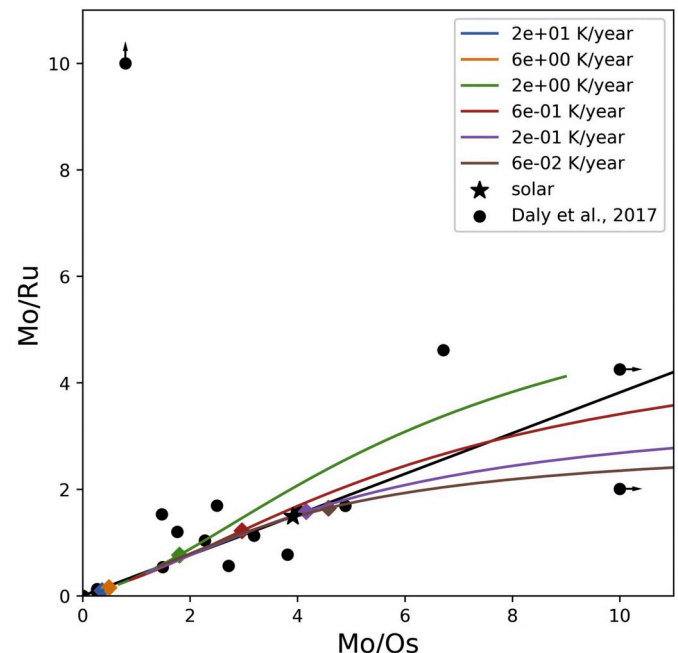

Fig. 14. Mo/Ru vs. Mo/Os of modeled RMNs condensing at different cooling rates, along with the data from Daly et al. (2017a). Diamonds represent the composition of the RMNs with highest number density. A point with horizontal arrow indicates that its Mo/Os is much larger than 10. A point with vertical arrow indicates that its Mo/Ru is much larger than 10.

temperature decreased exponentially, while this study assumed a linear decay of the temperature. Nevertheless, the cooling timescale in their study was equivalent to the reciprocal of the cooling rate defined in our study. Tanaka et al. (2002) models the kinetic condensation with the cooling timescale between 10^3 and 10^9 years, equivalent to the cooling rate between 10^{-3} and 10^{-9} K/year. Section 3.3 only shows the condensation temperature with the cooling rate above 0.05 K/year. Still the condensation temperature from Tanaka et al. (2002) is extrapolated to compare with this study. All refractory siderophile metals, except W, have lower condensation temperature in Tanaka et al. (2002) than those in this study. Os condenses homogeneously in both studies, but this study allows the heterogeneous condensation of other elements, leading to a larger grain size and faster condensation rate. Therefore, Os condenses faster and have higher condensation temperature in this study. Tanaka et al. (2002) did not consider the heterogeneous condensation of moderately refractory siderophile metals on preexisting RMNs, and their condensation temperature of Ir, Ru, Pt, and Mo was therefore underestimated. They also did not consider the oxidation of W, and its condensation temperature is overestimated. Lodders (2003) computes the equilibrium condensation temperature of refractory siderophile metals. NUCON also includes a module for equilibrium calculation and derives the equilibrium condensation temperature (Fig. 6). However, the temperature was slightly different from Lodders (2003) with deviation from 1 K (W) to almost 40 K (Mo), likely due to the difference in the input solar abundance. This study adopts the solar abundance from Lodders et al. (2009). Nevertheless, Lodders (2003) and this study have identical equilibrium condensation sequences of refractory siderophile metals.

This study shows that the kinetic inhibition from the high surface energy of refractory siderophile metals largely delays the condensation of refractory siderophile metals. Take Os as an example, the condensation temperature of Os has been decreased by around 300 K, from 1818 K to 1500 K at 10^{-4} bar, even with the cooling rate as low as 0.1 K/year. Thus, it is possible that RMNs might have condensed after other minerals in CAIs, like corundum and hibonite, whose equilibrium condensation temperatures are 1699 K and 1643 K (Yoneda and Grossman, 1995), respectively. It is possible that the condensation of oxide and silicate could also be inhibited by surface energy, but the inhibition may not be so significant because of the lower surface energy of oxide and silicate and higher partial pressure of rock-forming elements. Daly et al. (2017a) showed most RMNs in CAIs were found in spinel, melilite, perovskite, and anorthite. No RMNs have yet been found in corundum and hibonite, except in the molten CAIs from Schwander et al. (2015a). These petrological observations suggest that RMNs might have condensed later than corundum and hibonite.

4.7. The origin of Fe and Ni in RMN: diffusion or condensation?

The Ni/Fe ratio of an RMN can reflect the cooling rate during the condensation of Fe and Ni. One argument against this method is that Fe and Ni were not obtained by condensation but diffusion. This argument cannot stand for the following reasons: (1) Fe and Ni existed as gaseous phases at high temperature (> 1400 K). None of the solid forms of Fe and Ni could be stable at high temperature given the low pressure of the early Solar System. Even if Fe and Ni could form a solid solution, their concentration would be very low. If RMNs were captured by their host at high temperature, neither RMNs nor their host contained significant Fe and Ni, so diffusion, though rapid, would have little effect for RMNs to accumulate Fe and Ni. (2) After RMNs were captured by their host, the temperature decreases and the Fe and Ni started to condense on their host. Diffusion may transport Fe and Ni from the host to RMNs. However, it is hard to diffuse between the host mineral and the RMN. The host minerals in the CAI are usually spinel, melilite, hibonite, Al-diopside, and anorthite (Daly et al., 2017a). If these minerals provided a Fe atom during the diffusion, they should receive a Ca or Mg atom to maintain the stoichiometry. However, an RMN has little Ca and Mg, so

the inter-diffusion was unlikely to occur. (3) The metallic crystal structure of RMNs excludes grain boundary diffusion as the origin of Fe and Ni. In meteorites, grain boundary diffusion might account for the redistribution of Fe and Ni ions (Telus et al., 2016) in silicates. It required the Fe and Ni to be oxidized as ions, and they could be transported along cracks. Also, oxygen should be introduced through the diffusion process to maintain the charge balance. However, primitive RMNs have been observed to be pure metals and to contain little oxygen (Harries et al., 2012; Daly et al., 2017b), so the metallic Fe and Ni in RMNs should not come from grain boundary diffusion. (4) Grain boundary diffusion might carry Fe and Ni away from RMNs and modify their Ni/Fe ratio, but the existence of grain boundary diffusion could be inferred from the Fe, Ni-bearing cracks (Telus et al., 2016). Thus, an RMN should not be used to infer cooling rates if Fe, Ni-bearing cracks are found near it. It is hard to evaluate if an RMN has experienced grain boundary diffusion purely based on literature, because some literature may not provide the BSE image or petrological description of RMNs. However, some BSE images provided by literature (e.g., Daly et al., 2017ab) show that some RMNs and their host CAIs indeed have not experienced grain boundary diffusion.

4.8. Transition from slow cooling to rapid cooling

The radii and Ni/Fe ratios of RMNs suggest that RMNs should have experienced slow cooling first and then rapid cooling (Section 4.4). It is worthwhile to explore the transition where the RMN-forming region transited from slow to fast cooling. The temperature where the transition occurred is defined as "transition temperature" in this study. The behavior of Pt during both refractory-siderophile-metal and Fe—Ni condensation makes it a useful tool to constrain the transition temperature. At a high temperature when RMNs are formed, most refractory siderophile metals are supersaturated, but Pt has not yet reached saturation and only small amounts of Pt can condense on RMNs as solid solution (Fig. 3A). Thus, it takes relatively short time for Pt to reach equilibrium with the solar nebula (Fig. 3E). Fig. 6 shows that Pt condenses in equilibrium with the Solar Nebula even a cooling rate as high as 10 K/year during refractory-siderophile-metal condensation. It is almost impossible for the RMN-forming region to condense more rapidly than this rate during refractory-siderophile-metal condensation, because it will result in nm-scale RMNs (Fig. 8). On the other hand, when the Solar Nebula transitions to rapid cooling at moderate temperature, a large amount of Fe and Ni condense on RMNs in a few hours (Section 3.2.2.2). In this short timescale, little Pt can condense on RMNs due to its low partial pressure. Therefore, the abundance of Pt in RMNs are frozen at a rapid-cooling period and records the last moment of the slow-cooling period (Fig. 5A). The results from the modeling show that Pt has little time to condense on RMNs if the cooling rate exceeds 0.1 K/h during Fe—Ni condensation. Therefore, the concentration of Pt in RMNs should mark the endpoint of slow cooling, where the Pt of RMNs were in equilibrium with the Solar Nebula. Here I define the reduced fraction of Pt as the fraction of Pt over refractory siderophile metals, which should be a monotonic function of temperature, because Pt is the least refractory element among refractory siderophile metals and the fraction of Pt over refractory siderophile metals should increase with temperature decreasing. Here is the expression of the reduced fraction of Pt, $X_{Pt'}$,

$$X'_{\text{Pt}} = X_{\text{Pt}} \Big/ \sum X_{RM} \tag{17}$$

where X_{Pt} and $\sum X_{RM}$ are the molar fraction of Pt and the sum of the molar fraction of refractory siderophile metals, respectively. At high temperature, $\sum X_{RM}$ approximately equals to unity, so the reduced mole fraction of Pt can be approximated as,

$$X'_{\text{Pt}} \approx X_{\text{Pt}} = p_{\text{Pt,atom}} \Big/ p_{\text{Pt,sat}}(T_{\text{tran}}) \tag{18}$$

where $p_{\text{Pt, atom}}$ is the pressure of atomic Pt and $p_{\text{Pt, sat}}(T_{\text{tran}})$ is saturated

pressure of Pt at the transition temperature T_{tran}. When Fe and Ni started to condense, the concentration of Pt was diluted by Fe and Ni, but the reduced fraction of Pt should remain constant because little amount of refractory siderophile metals were available in the nebula to condense. Thus, the reduced fraction of Pt should be a robust tracer for the transition of cooling rate. The reduced fraction of Pt of an RMN can be obtained from its measured composition, and the transition temperature can be derived from Eq. (18).

The inferred transition temperature of the RMNs in the literature is shown in Fig. 15. Eq. (18) shows that the transition temperature is related to the pressure of Pt, which is proportional to the total pressure. Therefore, the inferred transition temperature is plotted in three sub-plots assuming that the RMNs formed in the pressure from 10^{-5} to 10^{-3} bar. Higher total pressure leads to higher inferred transition temperature. Some RMNs contain Pt with the amount below detection (<1 at.% for SEM/EDS), indicating that the transition might occur at high temperature, for example, over 1500 K at 10^{-4} bar. Some RMNs have a reduced fraction of Pt as high as 50%, suggesting that these RMNs were still in equilibrium with the nebular gas at around 1350 K at 10^{-4} bar. Most RMNs have a reduced fraction of Pt between 0 and 50%, so the inferred transition temperature is also around the range of 1350 and 1500 K at 10^{-4} bar. Thus, the assumption in this study that the transition takes place at 5% Ni saturation (1440 K at 10^{-4} bar) is reasonable in the first order. The RMNs from different studies (Wark and Lovering, 1976; Palme et al., 1982; Wark, 1986; Berg et al., 2009; Harries et al., 2012; Daly et al., 2017a) derive similar range of inferred temperature, and the RMNs from Harries et al. (2012) have relatively less Pt and derive the inferred temperature slightly higher than that from other studies.

If a group of RMNs have condensed from the same RMN-forming region, they should share the same reduced molar fraction of Pt because all of them were in equilibrium with the nebula until the transition from slow to rapid cooling. However, even the RMNs located in the same CAI have different reduced fractions of Pt (e.g. Daly et al., 2017a). One explanation is that the RMNs could have formed in different regions with different transition temperatures, and were later captured by the same host. Another possibility proposed by Daly et al. (2017a) is that RMNs could have condensed from the circumstellar environments with the heterogeneous composition from the solar nebula. If it was the case, the variety of Pt concentration in RMNs may be the result of condensation from circumstellar environments.

A future work of NUCON is to simulate the condensation of individual RMNs. It requires prior knowledge of the bulk composition of the system (nebula), transition temperature where the nebula transitioned from slow to rapid cooling, and the temperature where the RMN was captured. If the composition of RMNs is measured, their transition temperature can be derived from the reduced fraction of Pt, rather than being assumed arbitrarily. The moment an RMN was captured can be derived from the composition of Fe and Ni. The model can be set to be terminated when the modeled RMN has the same composition of Fe and Ni. The bulk composition is normally assumed to be solar composition, but the potential RMN-forming region could also include circumstellar environments.

4.9. Depletion of W in RMNs: result of kinetic condensation?

Equilibrium condensation has predicted that Mo and W should condense in RMNs along with other refractory siderophile metals given a canonical solar nebula. However, some RMNs were observed to lack W and/or Mo. Fegley Jr and Palme (1985) used thermodynamic computation to show Mo and W could be depleted in an oxidized solar nebula. Pristine RMNs could contain both Mo and W, but Mo and W would be lost during evaporation under oxidizing conditions. Their study showed that Mo was more depleted than W when the oxygen fugacity exceeded $1 \times fO_{2, \odot}$, but some RMNs in Daly et al. (2017a, 2017b) were found to contain Mo (> 10 at.%) and no W (< 1 at.%), which cannot be explained by evaporation under oxidizing conditions. This study provides an alternative way to explain the depletion of W. Since the condensation rate of gases is proportional to their partial pressure (Eq. (8)), and most W and some Mo exist as oxide gases in a canonical Solar Nebula (Fig. 2), the condensation rate of atomic W and Mo should be lower than other refractory siderophile metals. Fig. 3 shows 80% Mo and little W has condensed on RMNs at 1396 K when the total pressure, oxygen fugacity, and cooling rate are 10^{-4} bar, $1 \times fO_{2, \odot}$, and 0.15 K/year, respectively. Besides oxygen fugacity, cooling rate is also crucial for W and Mo condensation: low cooling rates will lead to equilibrium condensation, where Mo and W condense completely. However, Supplementary Information S6 shows that even with the cooling rate as low as 1.5×10^{-3} K/year, it still takes about 300,000 years for 50% W to condense. To be noticed, this example doesn't consider the nucleation inhibition from the surface energy of metals, and W starts to condense when it is saturated. At high temperature, W tends to dissociate as monatomic W and O gases. Thus, the condensation rate of atomic W would be higher at high temperature than that at low temperature. If the nucleation inhibition is considered, the start of RMN condensation will be delayed and the partial pressure of W would be even lower. It would take even longer time for W to condense. Therefore, in order to achieve equilibrium condensation for W, much slower cooling rate than 1.5×10^{-3} K/year is needed.

In Section 4.3, the reduced radii of RMNs are used to infer the cooling rates during refractory-siderophile-metal condensation. Most RMNs had
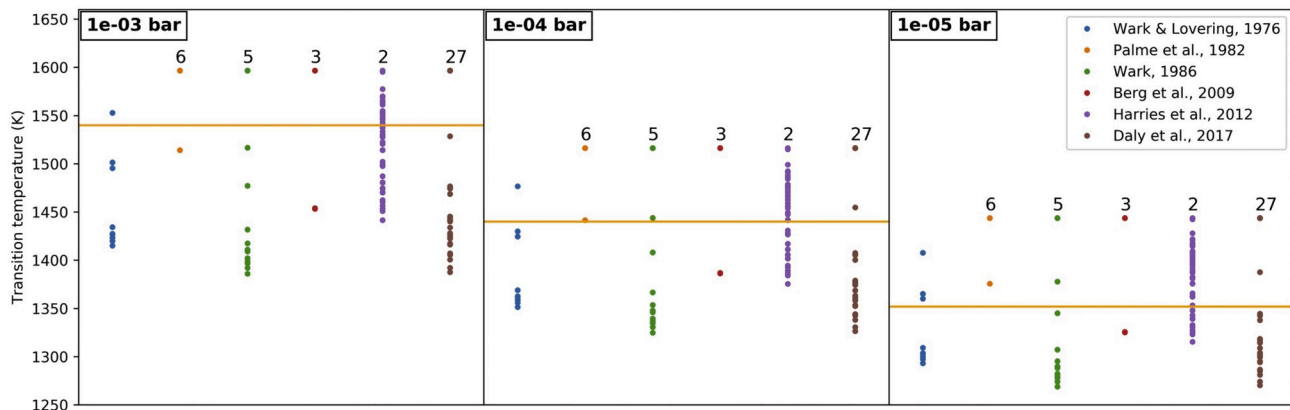
Fig. 15. The prediction of transition temperature from the Pt molar fraction of the RMNs in the literature. The Pt molar fraction can only infer the lower bound of the transition temperature if the concentration of Pt in an RMN is below detection (< 1%), and the numbers in the plot represent the number of RMNs that have undetected Pt and might have higher transition temperature. The orange horizontal lines mark the temperature used in Section 3 where RMN-forming regions transitioned from slow to rapid cooling.

their refractory siderophile metals condense with the cooling rate around 1 K/year. Given this cooling condition as well as the canonical Solar Nebula, over 50% Mo should have condensed at 1400 K at 10^{-4} bar, while most W should still remain as gases (Fig. 6B). This model successfully explains some RMNs consisting of Mo but without W (e.g. Wark and Lovering, 1976; Berg et al., 2009; Daly et al., 2017a). However, the RMNs consisting of both W and Mo (both >1 at.%) do exist (e.g. Wark and Lovering, 1976), which suggests that their formation regions could be much more reduced than a canonical solar nebula (Fig. 6E) or they may have been formed by precipitation (Schwander et al., 2015a).

The above discussion is based on an assumption that only atomic W can condense on RMNs. One may argue that W might condense through the dissociation of WO when it collides on the RMN surface, but it is limited by the high bond energy of W—O. Only the WO molecules with kinetic energy higher than the bond energy of W—O can break this bond and condense on RMNs, but the fraction of them is very low. The formation enthalpies of W(g), O(g), and WO(g) from the JANAF table (Chase, 1998) are used to estimate the bond energy of W—O, which is around 690 kJ/mol. Other studies also support this result (deB Darwent, 1970; Luo and Kerr, 2012). It is equivalent to the velocity of 2700 m/s for WO molecules. If the WO molecules obey the Maxwell-Boltzmann distribution, given the temperature of 1600 K, the fraction of such energetic molecules is lower than 10^{-9}. Therefore, it is almost impossible for the gaseous WO to dissociate and condense on the RMN.

5. Conclusion

NUCON, a kinetic model for condensation of metal from the Solar Nebula is developed, taking into account gaseous equilibrium, homogeneous nucleation, condensation, evaporation, and solid solution. NUCON has been used to simulate the formation of RMNs from a cooling Solar Nebula and infer the cooling history of the RMN-forming regions. Conclusions are summarized below:

1. The surface energy of refractory siderophile metals significantly inhibits the nucleation of RMNs. In the canonical Solar Nebula with pressure and cooling rate of 10^{-4} bar and 0.1 K/year, respectively, RMNs nucleate at the temperature at around 1500 K, which is over 300 K below the formation temperature of RMN in equilibrium condensation. Thus, the behavior of kinetic condensation of RMNs deviates largely from that of equilibrium condensation. Refractory siderophile metals (Os, Re, W, Ir, Mo, and Ru) have reached supersaturation at the nucleation of RMNs and condense kinetically.
2. The radius and Ni/Fe ratio of RMNs are sensitive to the cooling rate of Solar Nebula. Rapid cooling results in small-sized RMNs, vice versa. Besides, the pressure of RMN-forming regions also positively contributes to the radius of RMNs, while oxygen fugacity has limited influence on the radius. Ni/Fe of RMNs is insensitive to both pressure and oxygen fugacity of RMN-forming regions.
3. The radii of the RMNs from literature indicate that the RMNs could have accreted refractory siderophile metals through the kinetic condensation with a cooling rate in the order of 1 K/year. The timescale of refractory-siderophile-metal condensation is in the order of 10^2 years. The Ni/Fe ratios of the observed RMNs infer that RMNs could have accreted Fe and Ni with a cooling rate of higher than 1 K/h. The timescale of Fe—Ni condensation is in the order of 10 h. The dichotomy of the cooling rates between refractory-siderophile-metal condensation and Fe—Ni condensation indicates a transition from slow to rapid cooling in RMN-forming regions.
4. Due to the surface energy of refractory siderophile metals, the inhibition of nucleation largely delays the condensation of refractory siderophile metals. The most refractory siderophile metals (Os and Re) have their 50% condensation temperature over 300 K below the equilibrium condensation given a canonical Solar Nebula with pressure and cooling rate of 10^{-4} bar and 0.1 K/year, respectively.

However, Pt has 50% condensation temperature close to that of equilibrium condensation if the cooling rate is below 10 K/year.
5. Pt in RMNs could maintain equilibrium with Solar Nebula until the nebula transitioned from slow to rapid cooling. Thus, the concentration of Pt in an RMN can be used to derive the temperature where the transition occurred. The Pt abundance of the RMNs in literature suggests that the transition might have occurred from 1300 K to over 1500 K assuming the total pressure is 10^{-4} bar.
6. The condensation rate of an element is proportional to the fugacity of its monatomic phase. Since gaseous W and Mo exist mainly in oxide forms, their condensation rate is lower than other refractory siderophile metals, which may account for the absence of W and/or Mo in some observed RMNs.

Appendix A. Supplementary data

Supplementary data to this article can be found online at https://doi.org/10.1016/j.icarus.2020.113851.

References

Becker, R., Döring, W., 1935. Kinetische behandlung der keimbildung in übersättigten dämpfen. Ann. Phys. 416 (8), 719–752.

Berg, T., Maul, J., Schönhense, G., Marosits, E., Hoppe, P., Ott, U., Palme, H., 2009. Direct evidence for condensation in the early solar system and implications for nebular cooling rates. Astrophys. J. Lett. 702 (2), L172.

Blum, J.D., Wasserburg, G.J., Hutcheon, I.D., Beckett, J.R., Stolper, E.M., 1988. Domestic origin of opaque assemblages in refractory inclusions in meteorites. Nature 331 (6155), 405–409.

Borisov, A., Palme, H., 1995. The solubility of iridium in silicate melts: new data from experiments with Ir10Pt90 alloys. Geochim. Cosmochim. Acta 59 (3), 481–485.

Borisov, A., Palme, H., 1997. Experimental determination of the solubility of platinum in silicate melts. Geochim. Cosmochim. Acta 61 (20), 4349–4357.

Borisov, A., Walker, R.J., 2000. Os solubility in silicate melts: new efforts and results. Am. Mineral. 85 (7–8), 912–917.

Chase Jr, M.W., 1998. NIST-JANAF Thermochemical Tables. In: J. Phys. Chem. Ref. Data, 4th, 9. Monograph.

Connelly, J.N., Bizzarro, M., Krot, A.N., Nordlund, Å., Wielandt, D., Ivanova, M.A., 2012. The absolute chronology and thermal processing of solids in the solar protoplanetary disk. Science 338 (6107), 651–655.

Croat, T.K., Berg, T., Bernatowicz, T., Groopman, E., Jadhav, M., 2013. Refractory metal nuggets within presolar graphite: first condensates from a circumstellar environment. Meteorit. Planet. Sci. 48 (4), 686–699.

Daly, L., Bland, P.A., Dyl, K.A., Forman, L.V., Evans, K.A., Trimby, P.W., Ringer, S.P., 2017a. In situ analysis of refractory metal nuggets in carbonaceous chondrites. Geochim. Cosmochim. Acta 216, 61–81.

Daly, L., Bland, P.A., Dyl, K.A., Forman, L.V., Saxey, D.W., Reddy, S.M., Moody, S., 2017b. Crystallography of refractory metal nuggets in carbonaceous chondrites: a transmission Kikuchi diffraction approach. Geochim. Cosmochim. Acta 216, 42–60.

Daly, L., Bland, P.A., Saxey, D.W., Reddy, S.M., Fougerouse, D., Rickard, W.D.A., Forman, L.V., 2017c. Nebula sulfidation and evidence for migration of "free-floating" refractory metal nuggets revealed by atom probe microscopy. Geology 45 (9), 847–850.

Davis, A.M., Richter, F.M., 2014. Condensation and evaporation of solar system materials. In: Meteorites and Cosmochemical Processes, pp. 335–360.

deB Darwent, B., 1970. Bond dissociation energies in simple molecules. NSRDS-NBS 31.

Dillmann, A., Meier, G.E.A., 1991. A refined droplet approach to the problem of homogeneous nucleation from the vapor phase. The Journal of chemical physics 94 (5), 3872–3884.

Ebel, D.S., 2006. Condensation of rocky material in astrophysical environments. Meteorites Early Solar Syst. II 1, 253–277.

El Goresy, A., Nagel, K., Dominik, B., Ramdohr, P., 1977. Fremdlinge: potential presolar material in Ca-Al-rich inclusions of Allende. Meteoritics 12, 215.

El Goresy, A., Nagel, K., Ramdohr, P., 1978. Fremdlinge and their noble relatives. In: Lunar and Planetary Science Conference Proceedings, vol. 9, pp. 1279–1303.

Fedkin, A.V., Grossman, L., Ghiorso, M.S., 2006. Vapor pressures and evaporation coefficients for melts of ferromagnesian chondrule-like compositions. Geochim. Cosmochim. Acta 70 (1), 206–223.

Fedkin, A.V., Grossman, L., Humayun, M., Simon, S.B., Campbell, A.J., 2015. Condensates from vapor made by impacts between metal-, silicate-rich bodies: comparison with metal and chondrules in CB chondrites. Geochim. Cosmochim. Acta 164, 236–261.

Fegley Jr., B., Palme, H., 1985. Evidence for oxidizing conditions in the solar nebula from Mo and W depletions in refractory inclusions in carbonaceous chondrites. Earth Planet. Sci. Lett. 72 (4), 311–326.

Fischer-Gödde, M., Schwander, D., Ott, U., 2018. Ruthenium isotope composition of Allende refractory metal nuggets. Astron. J. 156 (4), 176.

Grossman, L., 1972. Condensation in the primitive solar nebula. Geochim. Cosmochim. Acta 36 (5), 597–619.

Grossman, L., 1973. Refractory trace elements in Ca-Al-rich inclusions in the Allende meteorite. Geochim. Cosmochim. Acta 37 (5), 1119–1140.

Grossman, L., Beckett, J.R., Fedkin, A.V., Simon, S.B., Ciesla, F.J., 2008. Redox conditions in the solar nebula: observational, experimental, and theoretical constraints. Rev. Mineral. Geochem. 68 (1), 93–140.

Harries, D., Berg, T., Langenhorst, F., Palme, H., 2012. Structural clues to the origin of refractory metal alloys as condensates of the solar nebula. Meteorit. Planet. Sci. 47 (12), 2148–2159.

Holzheid, A., Borisov, A., Palme, H., 1994. The effect of oxygen fugacity and temperature on solubilities of nickel, cobalt, and molybdenum in silicate melts. Geochim. Cosmochim. Acta 58 (8), 1975–1981.

Ireland, T.R., Fegley Jr., B., 2000. The solar system's earliest chemistry: systematics of refractory inclusions. Int. Geol. Rev. 42 (10), 865–894.

Komatsu, M., Fagan, T.J., Krot, A.N., Nagashima, K., Petaev, M.I., Kimura, M., Yamaguchi, A., 2018. First evidence for silica condensation within the solar protoplanetary disk. Proc. Natl. Acad. Sci. 115 (29), 7497–7502.

Krot, A.N., MacPherson, G.J., Ulyanov, A.A., Petaev, M.I., 2004. Fine-grained, spinel-rich inclusions from the reduced CV chondrites Efremovka and Leoville: I. Mineralogy, petrology, and bulk chemistry. Meteorit. Planet. Sci. 39 (9), 1517–1553.

Laaksonen, A., Ford, I.J., Kulmala, M., 1994. Revised parametrization of the Dillmann-Meier theory of homogeneous nucleation. Phys. Rev. E 49 (6), 5517.

Lodders, K., 2003. Solar system abundances and condensation temperatures of the elements. Astrophys. J. 591 (2), 1220.

Lodders, K., Palme, H., Gail, H.-P., 2009. Abundances of the elements in the solar system. In: Solar system. Springer, pp. 712–770.

Luo, Y., Kerr, J.A., 2012. Bond dissociation energies. In: CRC Handbook of Chemistry and Physics, vol. 89, p. 89.

MacPherson, G.J., 2014. Calcium-aluminum-rich inclusions in chondritic meteorites. In: Meteorites and Cosmochemical Processes, pp. 139–179.

Macpherson, G.J., Grossman, L., 1984. "Fluffy" type A Ca-, Al-rich inclusions in the Allende meteorite. Geochim. Cosmochim. Acta 48 (1), 29–46.

Palme, H., Wlotzka, F., 1976. A metal particle from a Ca, Al-rich inclusion from the meteorite Allende, and the condensation of refractory siderophile elements. Earth Planet. Sci. Lett. 33 (1), 45–60.

Palme, H., Wlotzka, F., Nagel, K., El Goresy, A., 1982. An ultra-refractory inclusion from the Ornans carbonaceous chondrite. Earth Planet. Sci. Lett. 61 (1), 1–12.

Palme, H., Borisov, A., Wulf, A.V., 1998. Experimental determination of the oxidation sequence of refractory metals. In: Lunar and Planetary Science XXIX.

Pan, M., 2019. Introduction to NUCON - a kinetic model for condensation from the solar nebula. In: Lunar and Planetary Science Conference, p. 1853.

Petaev, M.I., Wood, J.A., Meibom, A., Krot, A.N., Keil, K., 2003. The ZONMET thermodynamic and kinetic model of metal condensation. Geochim. Cosmochim. Acta 67 (9), 1737–1751.

Rudraswami, N.G., Prasad, M.S., Plane, J.M.C., Berg, T., Feng, W., Balgar, S., 2014. Refractory metal nuggets in different types of cosmic spherules. Geochim. Cosmochim. Acta 131, 247–266.

Rumble, J., 2017. CRC Handbook of Chemistry and Physics. CRC press.

Schwander, D., Kööp, L., Berg, T., Schönhense, G., Heck, P.R., Davis, A.M., Ott, U., 2015a. Formation of refractory metal nuggets and their link to the history of CAIs. Geochim. Cosmochim. Acta 168, 70–87.

Schwander, D., Buhre, S., Schönhense, G., Ott, U., 2015b. Synthesis of refractory metal nuggets and constraints on the thermal histories of nugget-bearing Ca, Al-rich inclusions. Meteorit. Planet. Sci. 50 (5), 893–903.

Sharp, Z., 2017. Principles of Stable Isotope Geochemistry. https://doi.org/10.25844/h9q1-0p82.

Stolper, E., Paque, J.M, 1986. Crystallization sequences of Ca-Al-rich inclusions from Allende: The effects of cooling rate and maximum temperature. Geochimica et Cosmochimica Acta 50 (8), 1785–1806.

Sylvester, P.J., Ward, B.J., Grossman, L., Hutcheon, I.D., 1990. Chemical compositions of siderophile element-rich opaque assemblages in an Allende inclusion. Geochim. Cosmochim. Acta 54 (12), 3491–3508.

Tachibana, S., Nagahara, H., Ozawa, K., Ikeda, Y., Nomura, R., Tatsumi, K., Joh, Y., 2011. Kinetic condensation and evaporation of metallic iron and implications for metallic iron dust formation. Astrophys. J. 736 (1), 16.

Tanaka, K.K., Tanaka, H., Nakazawa, K., 2002. Non-equilibrium condensation in a primordial solar nebula: formation of refractory metal nuggets. Icarus 160 (1), 197–207.

Telus, M., Huss, G.R., Ogliore, R.C., Nagashima, K., Howard, D.L., Newville, M.G., Tomkins, A.G., 2016. Mobility of iron and nickel at low temperatures: implications for 60 Fe–60 Ni systematics of chondrules from unequilibrated ordinary chondrites. Geochim. Cosmochim. Acta 178, 87–105.

Tyson, W.R., Miller, W.A., 1977. Surface free energies of solid metals: estimation from liquid surface tension measurements. Surf. Sci. 62 (1), 267–276.

Vitos, L., Ruban, A.V., Skriver, H.L., Kollar, J., 1998. The surface energy of metals. Surf. Sci. 411 (1–2), 186–202.

Wang, Y., Hua, X., WeiBiao, H., 2007. Petrogenesis of opaque assemblages in the Ningqiang carbonaceous chondrite. Sci. China Ser. D Earth Sci. 50 (6), 886–896.

Wänke, H., Baddenhausen, H., Palme, H., Spettel, B., 1974. On the chemistry of the Allende inclusions and their origin as high temperature condensates. Earth Planet. Sci. Lett. 23 (1), 1–7.

Wark, D.A., 1986. Evidence for successive episodes of condensation at high temperature in a part of the solar nebula. Earth Planet. Sci. Lett. 77 (2), 129–148.

Wark, D.A., Lovering, J.F., 1976. Refractory/platinum metal grains in Allende calcium-aluminium-rich clasts (CARC's): possible exotic presolar material?. In: Lunar and Planetary Science Conference, vol. 7.

Woolum, D.S., Cassen, P., 1999. Astronomical constraints on nebular temperatures: implications for planetesimal formation. Meteorit. Planet. Sci. 34 (6), 897–907.

Yoneda, S., Grossman, L., 1995. Condensation of CaO-MgO-Al2O3-SiO2 liquids from cosmic gases. Geochim. Cosmochim. Acta 59 (16), 3413–3444.